2023-12-18

# Mechanical Characterization of Vertically Aligned Carbon Nanotube Forest Microelectrodes for Neural Interfacing

Spencer McLeod Roberts
*Brigham Young University*

Mechanical Characterization of Vertically Aligned Carbon Nanotube Forest

Microelectrodes for Neural Interfacing


Spencer McLeod Roberts


A thesis submitted to the faculty of
Brigham Young University
in partial fulfillment of the requirements for the degree of

Master of Science


Robert Davis, Chair
Richard Vanfleet
Brian D. Jensen


Department of Physics and Astronomy

Brigham Young University

ABSTRACT

Mechanical Characterization of Vertically Aligned Carbon Nanotube Forest
Microelectrodes for Neural Interfacing

Spencer McLeod Roberts
Department of Physics and Astronomy, BYU
Master of Science

Silicon intracortical microelectrodes arrays (MEA) provide some of the best performance for brain computer interfaces but suffer from lifetime limitations that prevent clinical adoption. A primary contributor of lifetime limitations is the chronic foreign body response (FBR) which remains active in response to the brain tissue strain caused by implanted probes during brain micromotion. Designing probes with softer materials can reduce the chronic FBR and improve device lifetime. A high-aspect ratio CNT MEA could provide several advantages as an intracortical MEA but has yet to be mechanically characterized. CNT MEAs are infiltrated with 3 degrees of carbon infiltration and mechanically tested to determine their Young's modulus. A novel dual deflection (DD) test is designed to measure the cantilever bending of the CNT electrodes and determine their modulus. The CNT diameters of the microelectrodes are measured with SEM as a quantification method of carbon infiltration. A total of 64 CNT microelectrodes (MEs) are tested with the DD test and the modulus is calculated for a subset of 59 CNT MEs. The modulus results are grouped by infiltration level for statistical calculations. The DD test measured a mean modulus of $19.6 \pm 14.5$ MPa, $67.7 \pm 22.7$ MPa, and $168 \pm 62.3$ MPa for arrays fabricated with 0 second, 15 second, and 30 second infiltrations, respectively. A finite element analysis (FEA) model is developed to examine the brain tissue strain under a static, 10 μm, micromotion deflection of penetrating probes with the maximum (1.7 GPa), median (72 MPa), and minimum (3.9 MPa) CNT moduli we measured, as well as the modulus of silicon (165 GPa) for comparison. The max CNT and Si probes induced similar strain in the brain model at the probe tip, while the minimum and median CNT probes showed almost no strain at the tip. The model implies that for the CNT MEA probe geometry, significant reductions in the brain tissue strain can be achieved by CNT MEs with moduli in tens of MPa range, which can be fabricated with 15 seconds of carbon infiltration. Microelectrodes with 15 seconds of infiltration also demonstrated increased resilience compared to the other infiltration time groups, indicating that CNT MEAs with 15 seconds of infiltration might be a viable candidate material for a neural probe array.

ACKNOWLEDGMENTS

This work is the product of many years of labor by a host of individuals. First, I would like to thank my advisor, Dr. Robert Davis. Though initial contact was more difficult than I expected, he eventually offered me a rare opportunity to do cutting-edge research which ignited my love of microfabrication, carbon nanotubes, and neural implants. Dr. Davis taught me what it means to be a 'healthy skeptic' and cultivated my scientific scrutiny with countless tough questions. He has also been a leadership mentor and showed me how to cultivate the soft skills I need to be successful in all aspects of my life. I have enjoyed the copious hours chatting and writing together, though we both tend to get derailed easily. I can feel how invested he is in my success, which has made all the difference for me.

Likewise, I also want to thank my committee members, Drs. Brian Jensen and Richard Vanfleet. Both were invaluable in making this work a reality and were my close mentors and teachers. I acknowledge and express gratitude for the funding I have received from the BYU College of Physical and Mathematical Sciences and TULA Health. Their generosity allowed me to keep a project I cared deeply about alive long past its expiration date. I also would like to recognize and thank all the students of the Davis/Vanfleet lab that maintained the CNT furnaces and provided me with valuable insights. I especially want to thank Joseph Carter for his assistance with the FEA modeling. I would also like to acknowledge the invaluable support of the BYU Electron Microscopy Facility and the BYU Cleanroom Facilities who made this work possible.

Finally, I want to thank my wife and mother-in-law for pulling double duty with a new child while I slaved away at the keyboard. My wife is my biggest supporter and my partner in all my achievements.

# Table of Contents

# LIST OF FIGURES

# LIST OF TABLES

# 1. Introduction

## 1.1 Motivation: Neural interfacing

The future of brain computer interfaces relies on effective recording and stimulation devices. Penetrating intracortical probe arrays can provide the necessary signal to noise ratio, spatial resolution, and temporal resolution for effective brain computer interfaces. To be a viable brain implant, intracortical microelectrode arrays (MEAs) must satisfy at least four design requirements:

1. Geometry (electrode pitch, footprint, etc.).

2. Sufficient electrical properties (leakage current, impedance, and SNR).

3. Device robustness in the harsh environment of the body.

4. Biocompatibility, i.e., the host immune response does not impede device function.

The device performance specifications needed to meet these requirements depend on intended use, including animal research, human research, and clinical or commercial applications. Clinical devices must satisfy the requirements with high performance specifications for an extended period—ideally a decade—which has yet to be achieved with current technologies [1]–[6]. Clinically relevant specifications for each requirement will be briefly reviewed below.

The spatial and temporal resolutions required for a clinical intracortical device are defined by the anatomy and physiology of the brain. The cortex is the top surface of the brain where most of the computation in the central nervous system takes place. Most of the cortex is neocortex, which has six layers for input, output, and intracortical communication. These layers change in thickness and relevance depending on location, which is tied to function. For example,

the input layer IV of the primary visual cortex is significantly larger than in the primary motor cortex. The cortex is also folded into sulci and gyri to increase total cortical surface area. Generally, the computational units of the cortex are columns that are typically arranged perpendicular to the gyrus or sulcus and are spaced 300-400 µm apart. Intracortical MEAs are usually inserted on the flat part of a gyrus where the cortical columns align with the electrodes. Typically, neural implants target one electrode per input or output layer of a column, requiring at least a 400 µm pitch and a 1500 µm length [7]. However, these values should be seen as rule of thumb that is overruled by the specific anatomy of the target cortical area.

Electrical requirements of intracortical MEAs are determined by the firing rate of neurons in the target cortical area and the amplitude of immediate and local neural signals. Some neurons in the cortex can fire action potentials—which typically last ~1 ms—at frequencies as high as 500 Hz [7]. Intracortical arrays must not only be able to detect these spikes, but also sort them by shape, which requires sampling frequencies in the kHz range. Clinical MEAs will likely need to detect both single neuron spikes and neuron population signals, called local field potentials (LFP). LFPs are the temporal sum of many neurons' electrical behavior across a large area. As such, LFPs are lower amplitudes than individual action potentials, which measure in the µV and mV ranges, respectively [8], [9]. Intracortical MEAs also need to be low noise with an SNR of at least 1.5 [3].

The final two requirements, device robustness and biocompatibility, both contribute to device lifetime. Clinically relevant lifetimes vary depending on the quality-of-life improvement the device can offer to a patient. However, considering MEA implantation requires a craniotomy, the generally desired device lifetime is 5-10 years. The effective lifetime of a neural implant is determined by either device failure or loss of neural signal and should exceed desired lifetime.

Designing robust devices that can withstand the harsh environment of the body is non-trivial and is often a significant design limitation for neural implants [10]–[14]. On the other hand, loss of neural signal can happen independent of device failure and is the result of the host's immune response to the implant. MEA implantation triggers the brain's foreign body response (FBR), which recruits a variety of immune cells, microglia, and astrocytes to destroy or isolate the foreign body. Chronic activation of the FBR leads to gliotic encapsulation of the probes, nearby neuron death, device degradation, and ultimately, loss of neural signal [15]–[20]. Biocompatibility is the capacity of a device to mitigate the chronic FBR. Clinically relevant biocompatibility means the FBR is damped to the point that it does not isolate the device from healthy neuron signals over the desired lifetime of the device.

While no intracortical implant is ready for clinical use, the Utah Electrode Array (UEA) is a standout device which has been able to satisfy the four design requirements with sufficient performance to perform long-term human trials [21]–[25]. Developed by Richard Norman and colleagues in the 1970s, the UEA remains one of the most successful implantable neural multielectrode arrays, largely due to its high spatial resolution formfactor and impressive device lifetimes. The array is fabricated from a conductive silicon substrate through a series of dicing, etching, and encapsulations to produce a 10x10 silicon array. With 400 μm pitch between probes, the UEA can measure a planar map of cortical column activity at a specific cortical layer 1.5 mm deep. Originally, the UEA was designed to be implanted in the primary visual cortex to restore vision. The pitch and length of the probes were designed to stimulate the input layer IV in an array of cortical columns that corresponded to a map of retinal output [23]. Eventually UEA use expanded to enable cortical control of motor prostheses by recording signals in the output

layer V of the motor cortex, which was at a comparable depth to layer IV of the primary visual cortex [22].

To date, the UEA is the only intercortical MEA with FDA 510(k) approval that has been used in long-term non-human and human implantation studies [21], [26]. Sponheim *et. al.* reported in a meta-analysis of all reported *in vivo* studies with the UEA, that 16 out of 55 arrays met a 40% or greater electrode yield for over 800 days and three of those lasted for more than 5 years *in vivo* [3]. A single electrode was counted as "good" and contributed to the yield if it exceeded a SNR of 1.5. Encouragingly, two of the three long lasting arrays were implanted in a human subject. However, despite a few extended long-term recordings, 68% of the 51 implantations in non-human primates, were explanted due to signal loss. Sponheim *et. al.* observed that the arrays typically experience a ~2% drop in yield every 30 days, which reduced the number of viable arrays to 50% after one year of implantation [3]. Though these MEA lifetime yields are the best in the field, they still fall short of clinical specifications, indicating that there is still substantial room for lifetime improvement with UEA style implants.

A hypothesized cause of the long-term decrease in UEA electrode yield is insufficient biocompatibility, which results in the chronic foreign body response (FBR). The chronic FBR is mainly attributed to brain micromotion, where respiration, pulsation, and rotational acceleration of the head can displace a penetrating electrode by tens of microns relative to the tissue in the immediate vicinity [27], [28]. During this motion, the large mechanical mismatch between the stiff silicon electrode (~165 GPa) and the soft cortical brain tissue (~1-10 kPa) (see Figure *1*) can induce significant strain on the brain, which activates the chronic immune response and may even lead to neural tissue failure if greater than 0.1 in tension and 0.3 in compression [16], [18], [27], [29]–[33]. Soft biocompatible encapsulations and coatings on the UEA and other MEAs

have been explored to reduce the mismatch at the tissue-electrode interface, but to date, no coating has been demonstrated to have a significant impact on the long-term MEA biocompatibility [31], [34]. Long, thin, flexible alternatives to the UEA form factor have been made from polyimide (PI), parylene (PPX), and the epoxy based polymer SU-8 [35]–[38]. While the thin geometries of these probes offer lower stiffnesses, which have been shown to reduce the FBR, they are limited by their Young's modulus, which is still 6 orders of magnitude higher than brain tissue, as seen in Figure *1*. Additionally, the long-term robustness *in vivo* of these polymer probes has yet to be evaluated, or has fallen short of clinical requirements due to high gas permeability and water uptake [31], [35], [36], [39]. Therefore, exploring alternative materials and fabrication methods for UEA style implants that can improve the mechanical mismatch with brain tissue and still satisfy the other design requirements remains a viable area of research.
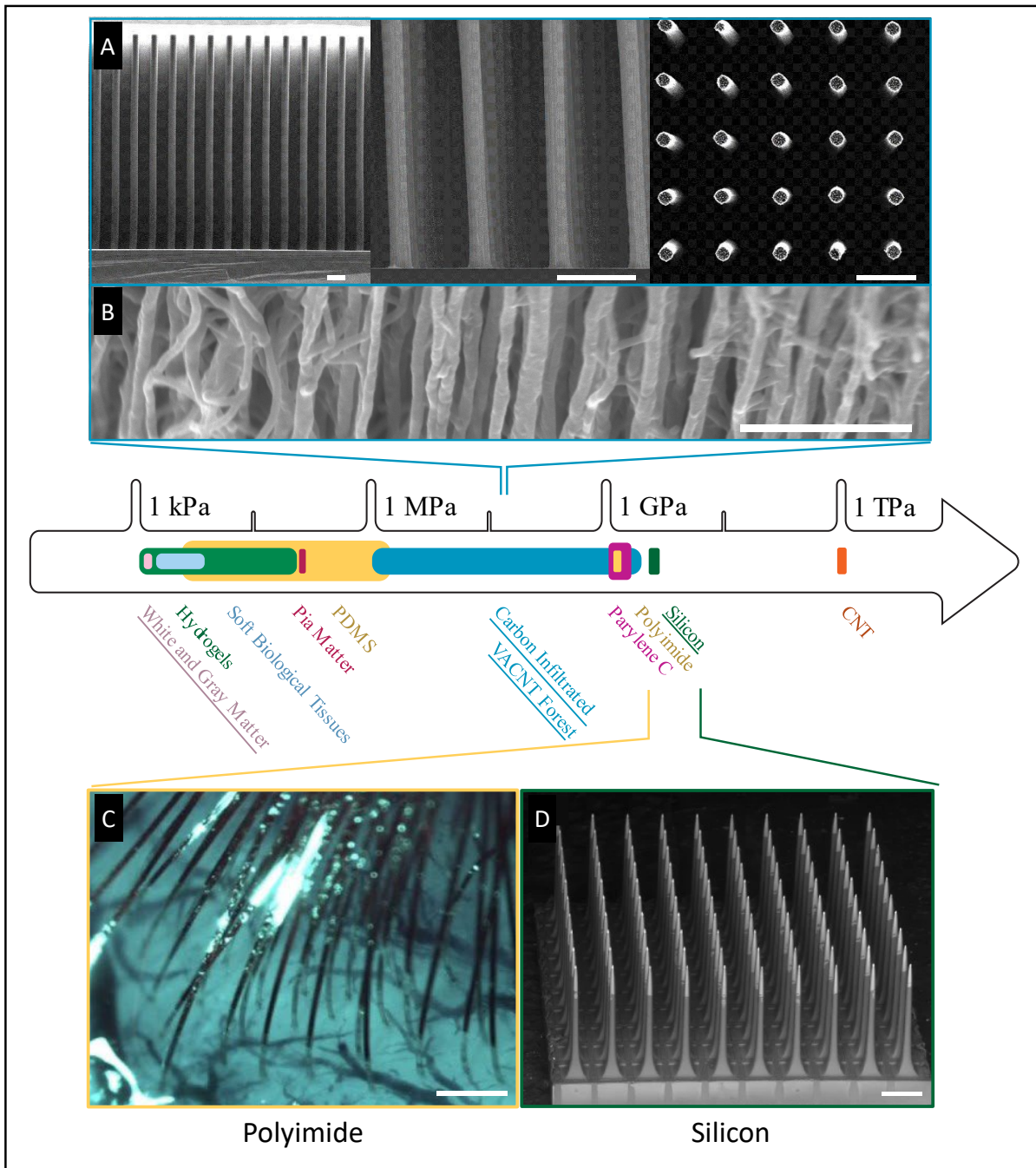
*Figure* **1**: *The large range of Young's moduli for materials relevant to neural implants with example devices. A) an electrode array fabricated from a carbon infiltrated vertically aligned carbon nanotube (CI-VACNT) forest. All scale bars are 400 microns. Adapted with permission from Chen et al. 2018. Copyright © 2018 American Chemical Society. B) a close-up SEM image of the carbon infiltrated VACNT forest. The scale bar is 500 nm. C) polyimide neural array produced by Neuralink after implantation in cortex. Scale bar is 500 microns (Musk et al. 2019). Reprinted under CC license. D) silicon Utah electrode array (UEA). The scale bar is 400 microns. Reproduced with permission from Springer Nature (Bhandari et al 2010).*

## 1.2    Carbon Nanotube Microelectrode Arrays for Neural Interfacing

Carbon nanotube templated microfabrication (CNT-M)  is a promising alternative MEA fabrication material and technique that could meet all the design requirements with possibly higher performance than the UEA [40], [41]. Chen *et al*. demonstrated a CNT MEA with sufficient spatial resolution for clinical applications. They reported the fabrication of a millimeter tall CNT forest microelectrode array (MEA) with microelectrodes 20 µm in diameter and a reduced pitch of 100 µm, compared to the UEA's traditional 400 µm pitch [42]. To achieve such high aspect ratios, the array must be locked into a self-supporting grid during growth with "sacrificial hedges" to ensure straightness. These sacrificial hedges must be removed after growth using a multistep plasma etching process that frees the microelectrodes (MEs) and narrows them to the free-standing structure in Figure 2-b. However, this etching process is laborious and produces a tight 100 µm spacing between MEs, which is not enough room to do mechanical testing. The mechanical properties of the high-aspect ratio CNT MEA were not evaluated by Chen *et al*. To measure the modulus of the CNT MEA in this work, we opted to use shorter, unsupported MEs that do not require plasma etching and have wider 400 µm spacings.
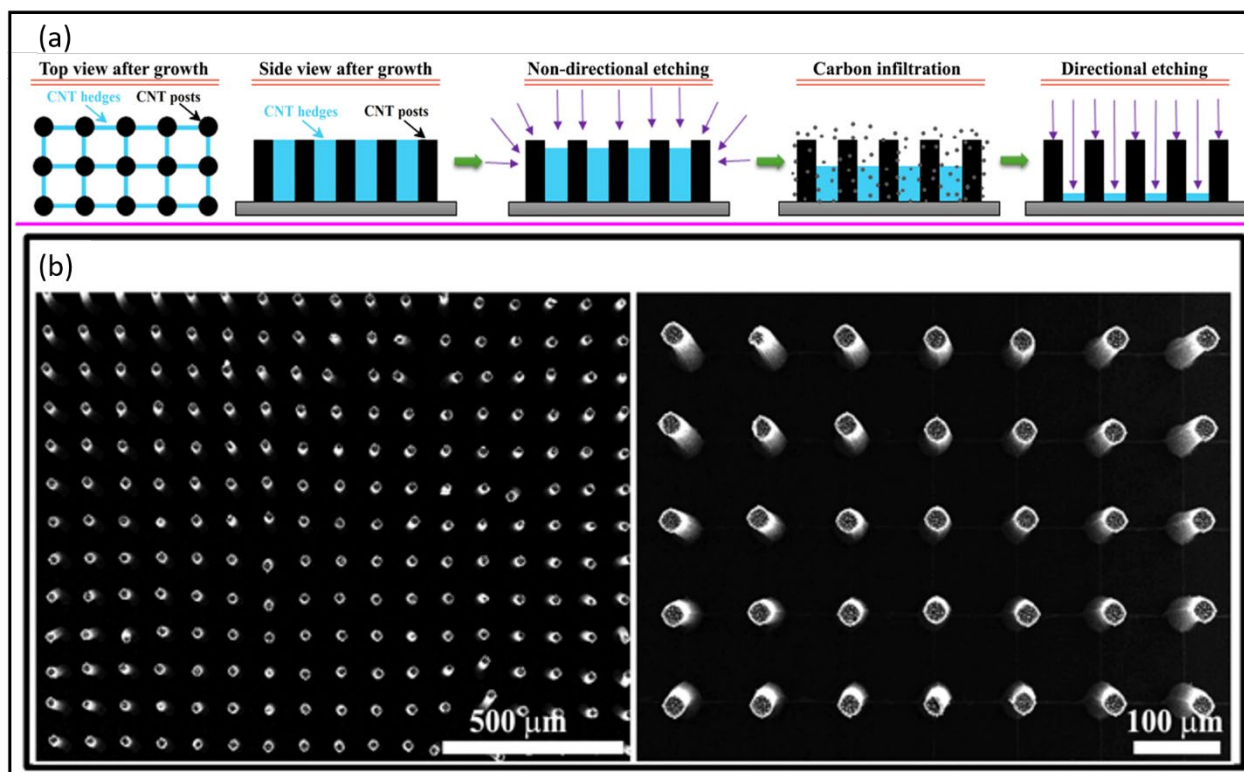
*Figure 2*: *The fabrication process of the high aspect ratio CNT MEA. a) The plasma etching process to remove the support hedges. b) The processed CNT MEA with free standing, straight, millimeter tall electrodes after plasma etching. Adapted with permission from Chen et al. [42]. © 2018 American Chemical Society.*

CNTs also have excellent electrical properties, and have been used in various biosensor designs [18], [43], [44]. CNT forest structures have high surface areas that decrease impedance and improve signal to noise during neural recordings [45]. Additionally, CNT electrodes are capable of monitoring neurochemical levels with cyclical voltammetry (CV) [43], [46]. Because of their chemical inertness, CNTs are robust and not prone to degradation *in vivo* and have even been shown to be resistant to dopamine fouling during CV measurements [47].

Unfortunately, the biocompatibility of CNTs is not well defined and contradictory results are often reported in the literature. The heterogeneity of CNT structures makes it difficult to generalize one CNT toxicity study to CNTs produced under different conditions. Many studies in the 2000s and early 2010s reported cytotoxic and carcinogenic properties to individual CNTs,

especially upon pulmonary inhalation [48]–[51]. By the late 2010s a more nuanced picture of CNT biotoxicity was revealed as the complexity of factors inducing toxicity and subsequent mitigating methods, such as functionalization, were discovered [43], [50], [52]–[54]. Additionally, researchers began investigating the biocompatibility of implanted CNT structures, which were often better received by the body than unstructured CNTs that were injected or inhaled [55], [56]. Some works even reported no toxicity or biocompatibility with mammalian biology [47], [57]–[60]. For example, some studies have reported that CNTs promote neurite growth and neuron cell adhesion, improving neural recording signals [61]. Considering the diversity of CNT properties and toxicity results, the biocompatibility of CNT based devices must be evaluated on a per device basis by mechanical characterization and *in vitro* or *in vivo* cell histology. Since the CNT MEA is an implanted structure and as stated before, brain micromotion can be a main cause of the chronic FBR, modeling strain on brain tissue by the CNT MEA is a reasonable first approximation of CNT MEA biocompatibility.

## 1.3   Summary of This Work

To determine the strain on brain tissue by CNT electrodes during micromotion, this work measured the effective Young's modulus of high-aspect ratio CNT electrodes over a range of carbon infiltration conditions. We also used finite element analysis to model the effect of the measured moduli range on brain tissue strain during probe micromotion. The electrodes measured were 40 µm in diameter and about half a millimeter in length, so traditional three-point bending tests were not feasible and a unique micro "dual deflection" (DD) method was developed to measure the moduli the CNT MEs. The DD test used a microwire of known stiffness to measure the unknown stiffness of 64 CNT MEs. Since CNT neural arrays might need to be strengthened for brain insertion, we carbon infiltrated some arrays at 900°C and separated

results by the following infiltration conditions: 0 seconds (no infiltration), 15 seconds, and 30 seconds. The average nanotube diameter per ME was measured by SEM as an alternative quantification of carbon infiltration. We expected both CNT diameter and Young's modulus to rise with increased infiltration time. We also expected Young's modulus to increase as CNT diameter increases. The modulus results were plotted on a log scale vs CNT diameter and grouped by infiltration time. Dual axis boxplots of the results showed a positive trend between infiltration time and both CNT diameter and Young's modulus, which was expected. The measured moduli of the CNT MEs ranged from 3.9 MPa to 1.7 GPa +/- 34% with the uninfiltrated MEs being measuring the lowest and the 30 second carbon infiltrated MEs measuring the highest, demonstrating that high-aspect CNT electrodes can be fabricated with a large range of moduli.

After measuring the moduli of 64 MEs, a FEA model of a deflecting probe in brain tissue was developed to assess the impact of the measured CNT moduli range on brain tissue strain compared to a silicon probe. We used the minimum, median, and maximum of the measured CNT electrode moduli and the moduli of silicon for our comparison. The FEA results indicated that regardless of moduli, a static, 10 µm deflection, induces strains close to 0.1 at the surface. However, 1.7 GPa CNT, 72 MPa CNT and 165 GPa silicon probes exhibited minimum bending and fulcrumed in the tissue to induce strain at the tip, while the lowest CNT modulus of 3.9 MPa bent easily and quickly dissipated the strain induced by the surface deflection. Our model shows that for probes 20 µm in diameter and 1000 µm in length, the modulus must be in the tens of MPa range—which our CNT MEs achieved—to induce almost zero strain at the tip recording site. In conclusion, high aspect CNT electrodes have been fabricated over a range of moduli and

have been shown to reduce brain tissue strain compared to the silicon probes, thus meriting

further investigation into high-aspect ratio CNT MEAs for neural interfacing.

## 1.4    Tools Used for This Work

### 1.4.1    Carbon Nanotube Microfabrication

The CNT microfabrication (CNT-M) can produce extremely fine, sharp structures that

can function as micro-electro-mechanical systems (MEMS). This section will review the nature

of CNTs, the general process of CNT growth and infiltration, and a review of literature that

measured the Young's modulus of CNT structures.
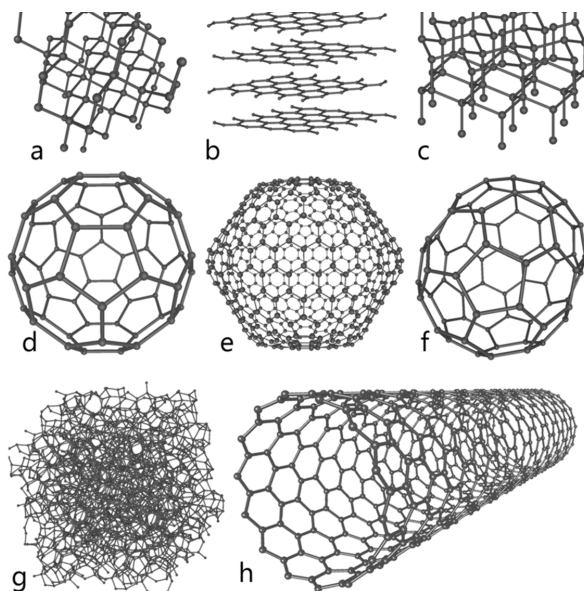


*Figure 3*: *Left: Eight of the allotropes (different molecular configurations) that pure carbon can take: a) Diamond b) Graphite c) Lonsdaleite d) C60 (Buckminsterfullerene) e) C540 f) C70 g) Amorphous carbon h) single-walled carbon nanotube. Credit Michael Ströck [62]. Reprinted under CC license.*

A CNT is a unique allotrope, or chemical alignment, of pure carbon atoms. It is

composed of repeating hexagonal units and resembles a graphene sheet—shown in Figure 3-b—

that has been rolled into a tube. There are two types of CNTs: single-walled carbon nanotubes

(SWCNT) and multi-walled carbon nanotubes (MWCNT). A SWCNT is depicted in Figure 3-h

and consists of a layer of carbon atoms, while a MWCNT is composed of concentric nanotubes of increasing diameter. These two classes of CNTs have different attributes and grow under different conditions, but all CNTs possess many unique and desirable qualities, such as: electrical conductivity, extreme strength-to-weight ratios over 100 times greater than high-carbon steel, high optical absorption, and good thermal conductivity [63]. Growth conditions can be tuned to control these properties by altering how many walls the tube has and its chirality, *i.e.*, the angle of the graphene wall of the CNT. While individual nanotubes are fascinating materials, this work utilizes CNTs grown as a tight knit "forest", which can be based off any two-dimensional pattern with techniques detailed later in this section. These forests allow for the fabrication of the tight dimensions necessary for MEMS and take advantage of CNT electrical conductivity on a microscale. Figure 4, a CNT forest in the shape of the BYU logo, shows the complex patterning capability of CNT MEMS as well tight dimensional control and fine features.
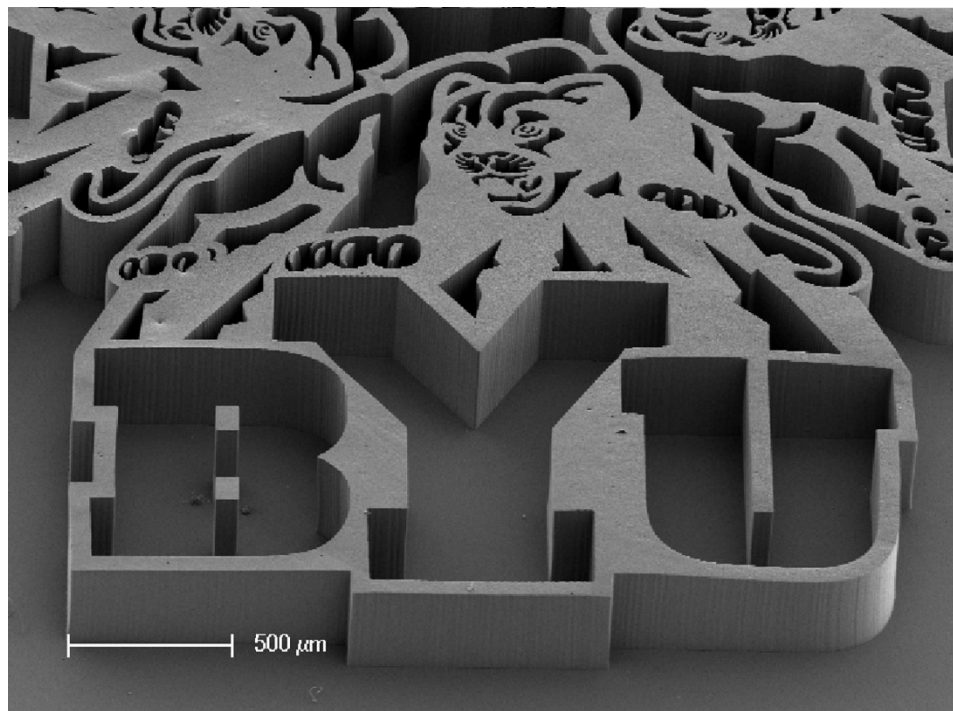


*Figure 4:* A carbon nanotube forest patterned in the shape of the BYU logo. Design modified and picture taken by Taylor Wood. Reprinted with permission from Song et al. [64]. © Wiley 2011.

Carbon nanotube growth is sensitive to many parameters, especially the nature of the thin film stacks on the growth substrate. CNT-M relies on specific thin film stacks for patterned CNT growth, which are shown in Figure 5. The orange film shown in Figure 5 is a catalytic metal on the surface of the stack upon which CNTs grow. The catalyst must be thin for CNT growth to occur: between 1 and 10 nm. In our method, we used 2 nm of iron—the most common CNT catalyst—for CNT growth. Evidence has shown that there when the iron layer is thinner, the CNTs grow fast and die young and that relationship inverts as the iron gets thicker [65]. The growth process occurs between 750˚C and 760 ˚C, at which temperature range the iron begins to form small droplets on the surface. Similar to soap bubbles on the surface of water, the larger iron droplets begin to grow at the expense of the smaller ones, consolidating the iron into large droplets; this process is called Ostwald Ripening [66]. The larger the droplet, the larger the diameter of the CNT that grows from them. Thicker iron layers promote larger droplets, resulting in larger CNT diameters.
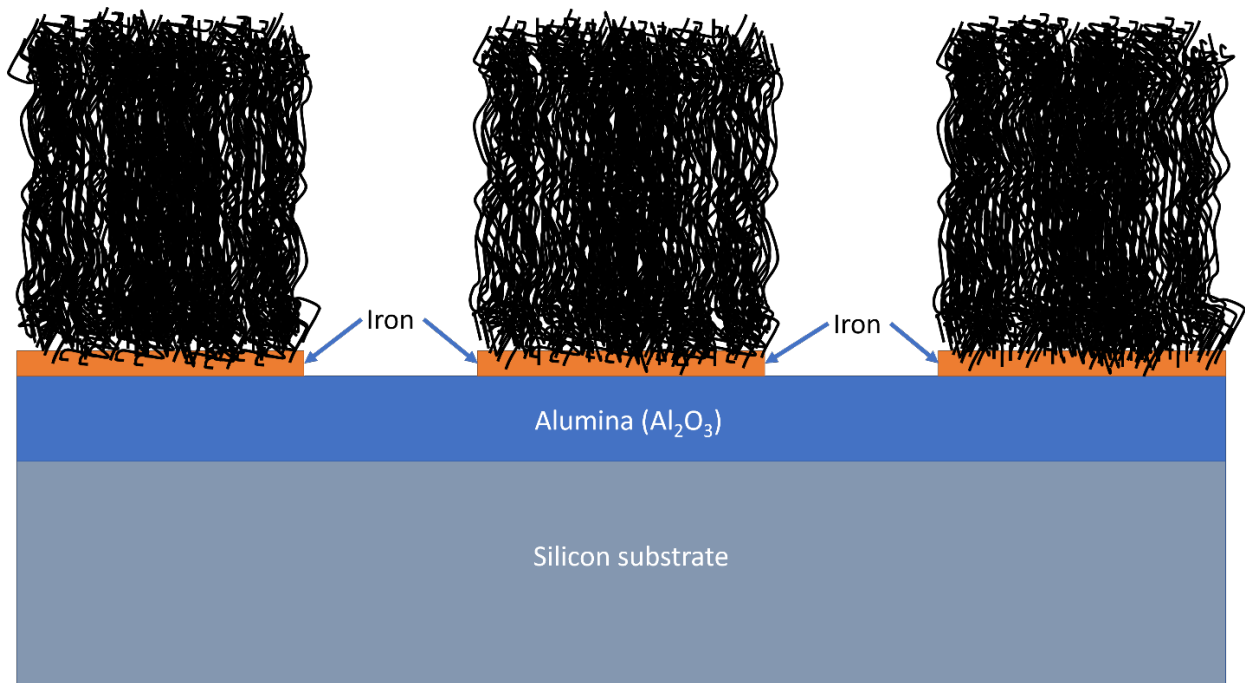


*Figure 5: A depiction of the thin film stack required for CNT MEMS growth. The CNTs grow directly out of the iron.*

Beneath the iron is an alumina layer that helps prevent the diffusion of the iron droplets laterally and into the layers below them, which terminates growth. Without the alumina barrier, the iron would quickly diffuse into the silicon when exposed to heat. The alumina slows this diffusion process, keeping the iron on the surface long enough for carbon nanotubes to form. CNT forests are usually grown on a standard commercial grade silicon wafer, though other substrates that can withstand high temperature, such as quartz, can be used. Approximately 30 to 40 nm of alumina is deposited on the silicon via electron beam (e-beam) evaporation or sputtering. The alumina layer is an important diffusion layer between the silicon wafer and the iron film on which the CNTs grow.

Once the alumina layer is deposited, the catalytic iron layer can be deposited. If iron is deposited over the entire surface of the alumina, then CNTs will grow over the entire surface, making a "blanket" forest without any patterns or features. If a patterned forest is desired, like Figure 2 and Figure 4, then traditional photolithography methods are used. The silicon/alumina stack is coated in AZ3030, a positive photoresist, then exposed to UV light through a patterned mask that casts a shadow in the shape of the desired 2D growth pattern. The wafer is immersed in developer which removes the unexposed photoresist, leaving behind holes in the pattern. Iron is then deposited on the wafer and the remaining photoresist is removed with an organic solvent (NMP). The result is a silicon/alumina/iron stack where the iron is patterned in a top-down view of the desired 3D structure. The CNTs will grow directly from the patterned iron.

The Fe/Si/alumina stack is processed in a CVD oven in a one-inch inner diameter quartz tube at 760°C with ethylene and hydrogen gas flown at 238 and 262 sccm, respectively. the hydrogen continually flows over the silicon chip during ramp up to 760°C, reducing the iron on the surface in preparation for CNT growth. Once the target temp of 760°C is met, ethylene flows

as a carbon feed stock gas, undergoes pyrolysis and diffuses into the iron nanoparticles. The carbon then precipitate out of the iron in nanotube form [67], [68]. With 2 nm of iron, CNT structures up to one mm height can be grown in 15 minutes. Once the target time is met, the system is cooled under argon flow and the array is removed. The resulting array is a 3D CNT projection of the 2D photolithographic pattern, as seen in Figure 2, Figure 4 and Figure 5. Finally, the CNT structures can be strengthened with carbon infiltration. As grown, the CNT forest is mostly void, which can make it fragile. Filling the voids to some degree with amorphous carbon greatly strengthens the structure so that it can survive mechanical testing. Infiltration is done with the same growth conditions but at higher temperatures between 800˚C and 900˚C.

The moduli of CNT forests infiltrated with carbon at 900˚C were evaluated by Hanna *et al.* and Laughlin *et al.* Their results highlight the importance of considering not only infiltration time, but also CNT diameter or iron thickness and the anisotropic alignment of CNT forests when making mechanical measurements of CI-CNT structures. Hanna *et al.* and Laughlin *et al.* both measured the Young's modulus of highly carbon infiltrated CNT structures with 3-point bending and cantilever bending methods [69], [70]. Since CNT forests are vertically aligned, the magnitude of the measured Young's modulus likely depends on the direction of the force relative to the CNT alignment. With this consideration, Hanna *et al.* measured modulus with stress both parallel and transverse to the nanotube alignment, while Laughlin *et al.* only measured modulus with transverse stress. We will use the terms "parallel Young's modulus" to refer to the value determined by mechanical tests where the stress is parallel to the nanotube alignment and "transverse Young's Modulus" to refer to the value determined by mechanical tests where the stress is transverse to the nanotube alignment. Hanna *et al.* reported that for nanotubes grown with iron thickness ranging from 4 to 10 nm—this study used 2 nm—the transverse Young's

15

modulus ranged from 4.1-8.6 GPa and 7.4-15.7 GPa with infiltration times of 30 and 120 minutes, respectively. The parallel Young's modulus of 11 GPa was measured with structures grown on 3 nm of iron and infiltrated for 30 minutes. Laughlin *et al.* reported a transverse Young's modulus ranging from 60 kPa to 7000 kPa (7MPa) for uninfiltrated structures and structures with 5 minutes of infiltration, respectively. Laughlin's structures were grown on 1 nm of iron with CNT diameters measuring ~4 nm before infiltration and ~21 nm after 5 minutes of infiltration.

### 1.4.2   Euler Beam Theory

The theoretical basis for measuring beam stiffness using deflection under force is the Euler beam theory, which is used in this work to measure the stiffness of CNT MEs. This beam theory applies only to small beam deflections under lateral loads, which are the conditions used to test the MEs as detailed in section 2.5. The theory starts by relating the bending moment to the curvature or deflection of the beam. The bending moment equation is a well-known and important to engineering and for those interested, there is full derivation on Wikipedia [71]. The bending equation is shown in equation 1, where $M$ is the bending moment, $E$ is the elastic modulus of the beam, $I$ is the second moment area of the beam's cross-section, and $\frac{\partial^2 y}{\partial x^2}$ is the second derivative of the beam deflection with respect to some position $x$.

$$M = -EI \frac{\partial^2 y}{\partial x^2} \qquad\qquad 1$$

For cantilevered beam—a beam that is clamped at one end—the bending moment is also equal to equation 2, where $F$ is the lateral force on the end of the beam, $L$ is the length of

the beam and $x$ the distance from the clamp to the end of the beam. From eq. 2, we see that the

bending moment is maximum at the base of the beam and zero at the end of the beam.

$$M = -F(L - x) \qquad\qquad 2$$

By setting equations 1 and 2 equal to each other, integrating, and evaluating at

$x = L$, the free end deflection is obtained in equation 6.

$$\frac{\partial^2 y}{\partial y^2} = \frac{F}{EI}(L - x) \qquad\qquad 3$$

$$\iint \frac{\partial^2 y}{\partial x^2} = \iint \frac{F}{EI}(L - x)\,dx^2 \qquad\qquad 4$$

$$y = \frac{F}{6EI}(3Lx^2 - x^3) \qquad\qquad 5$$

$$y = \frac{FL^3}{3EI} \qquad\qquad 6$$

Now by Hooke's law, the stiffness of a spring is the force applied to it divided by

the distance that it the spring deflects. Therefore, equation 6 is easily rearranged to find the

elastic modulus with respect to the beam's stiffness, $k$.

$$E = k\frac{L^3}{3I} \qquad\qquad 7$$

Finally, the second area moment, $I$, for a beam with a circular cross-section, is

equal to $\frac{\pi d^4}{64}$, where $d$ is the diameter of the beam. This substitution yields equation 8, the final

description of the beam's elastic modulus with respect to stiffness. However, for our experiment,

the only experimentally measured values are deflections. Therefore, we will include force and

deflection in our final result, as shown in equation 8.

17

$$E = \left(\frac{F}{y}\right)\frac{64L^3}{3\pi d^4} \qquad\qquad 8$$

# 2. Methods

## 2.1 CNT ME Fabrication and Infiltration

The CNT microelectrode array was fabricated following the methods detailed by Chen *et al.* with a few modifications. The pitch between MEs was increased from 100 μm to 400 μm to match the UEA and to allow for more area for mechanical testing. Additionally, to simplify the fabrication process, the MEs were grown as freestanding structures without the need for a support grid or plasma etching. Because no plasma etching was used, the ME diameter remained 40 μm and did not narrow to 20 μm as in the Chen *et al.* paper. To ensure straightness, the MEs were grown with a target length of 600 μm or lower, though length did vary between 280 and 750 microns between growths. The lengths of the MEs were measured with optical microscopy with an uncertainty of +/- 5 microns. MEs whose tips and base did not overlap when viewed normal to the substrate, caused by non-vertical growth, were not used in testing. Consistent with Chen *et al.*, all MEs were cylindrical.
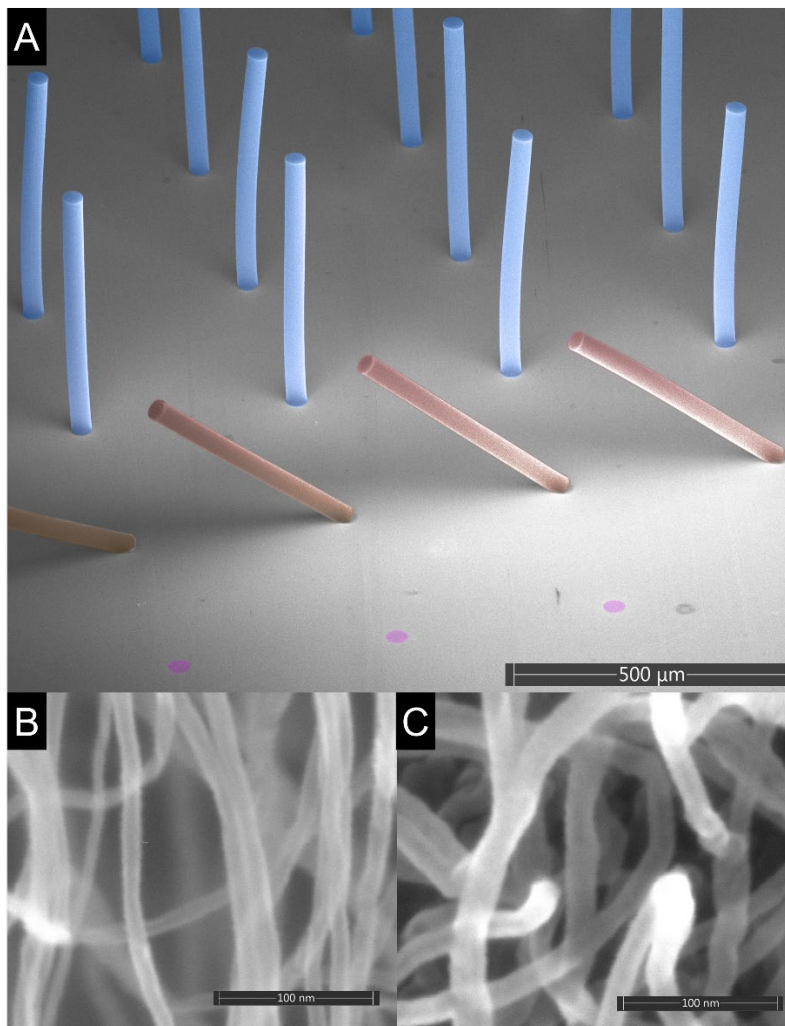
*Figure 6: SEM images of the CNT array. A) and overview of the array after the DD test. The Blue MEs are untouched, and the red have been knocked over during testing. The magenta circles in the foreground are the footprints where previous MEs have already been removed. B) a close-up of uninfiltrated CNTs in a CNT ME. Images like this were used to measure the CNT diameter. C) a close-up of 30 sec infiltration CNTs in a CNT ME.*

The arrays were grown via a carbon nanotube microfabrication (CNT-M) process using

carbon infiltration which is explained in detail by Fazio *et al.,* Chen *et al.,* and section 1.4.1 of

this work [40], [42], [69].  To briefly summarize the process, a 2 nm catalyst of iron was

patterned on a 30 nm alumina layer on a 1 $cm^2$ silicon substrate. To induce CNT growth The

Fe/Si/alumina stack was processed in a CVD oven in a one-inch inner diameter quartz tube at

760°C for 15 minutes with ethylene and hydrogen gas flown at 238 and 262 sccm, respectively.

Following growth, two subsets of arrays were infiltrated with carbon for 15 and 30 seconds to

increase their modulus. Carbon infiltration was achieved in the same CVD furnace at 900°C with ethylene and hydrogen flow rates of 337 and 310 sccm, respectively. To help characterize the infiltration and growths, the CNT diameters were measured by SEM at one micron from the base of the MEs before (Figure 6-B) and after infiltration (Figure 6-C). At least 10 tube diameters were measured and averaged per array.

## 2.2   Mechanical testing

The mechanical testing of the CNT MEs was achieved with a method we will call Dual Deflection (DD). The DD test uses deflections of two simple cantilever beams in contact with each other—one cantilever of known stiffness (we use a calibrated wire) and one of unknown stiffness (the CNT ME)—to determine the Young's modulus of the unknown beam. Measurement of the deflections is performed under an optical microscope and recorded for later analysis. Using the known stiffness of the wire, the dimensions of the CNT ME, and the observed deflections of the beams, the Young's modulus of the CNT ME is calculated. This DD method is ideal for beams that are too small for traditional 3-point bending measurements, like our CNT MEs. Figure 6.A shows a CNT array where the first row, false-colored red, has been tested with the DD method. The DD test can be destructive, evident by the red MEs resting at an angle, partially detached from the substrate. The rows of MEs false-colored blue have not been tested.

Due to the small size of the beams, the DD test must be performed under a microscope for both micromanipulation of the beams and accurate recording of the deflections. The CNT ME substrate is placed on the optical microscope stage and the wire is suspended in space above the stage (see Figure 7.A). The microscope stage is moved laterally to bring the ME into contact with the wire, then—after pausing motion to ensure contact and let vibrations settle—the substrate is moved further laterally to force the cantilevers together and induce bending of both

20

beams (see Figure 7-C) until the ME breaks off the substrate or deflects enough that the wire

slips off, events that we will refer to as DD test conclusion. To ensure ME deflections of at least

10 μm before the wire slips off, the wire contacted the ME an average of $175 \pm 75$ μm from the

top of the ME. The deflections of the wire and ME are observed and recorded through the

microscope in 4K resolution at 60 fps. Figure 7-B shows the overhead microscope view of the

DD test. Because the wire is fixed in space relative to the microscope and the array containing

the MEs is moved, a reference ME must be in the same view as the target ME/wire deflection to

determine the ME deflection. A non-physical, not to scale, 3D representation of the wire/ME

interaction and the measured quantities are shown in Figure 7-C. After the DD test, the wire

deflection and reference displacement, $y_w$ and $x_{ref}$, respectively, are measured using computer

vison tracking. The resulting data is processed with a python script which calculates the ME

deflection, $y_p$, as shown in equation 11. The script then plots the wire and ME deflections against

each other (Figure 15-A), removes any offset, performs total least squares regressions (TLS) on

the deflection plots to account for the uncertainty in each variable (Figure 15-B), and uses the

resulting slope to solve for the Young's modulus of the CNT ME as shown in equation 8 (Figure

15-C and Figure 15-B).

The known beam stiffness should be on the same order of magnitude as the beam of

unknown stiffness, so that the deflections of each beam are on the same scale and can be

observed optimally at the same magnification. This can be determined empirically by attempting

the DD test with known beams of different lengths. This work used several small straight

segments of Stableohm 650 wire from California Fine Wire, ranging between 2.5 to 4.6 mm in

length, as the known beam. The wire was secured with adhesive to a larger wire for handling and

mounting to a 3-axis stage. The length of the wire was measured optically with an uncertainty of

+/- 10 microns. The diameter of the wire provided by the manufacturer as 20 μm with an

uncertainty of +/- 1.27 microns was verified with a digital micrometer and optical microscopy.

During the DD test, the point of contact of the wire with the CNT ME was measured optically

and the wire lengths and ME lengths were adjusted accordingly for the calculations. The

Young's modulus of the wire was reported by the manufacturer as 213.7 GPa with an uncertainty

of 1%.
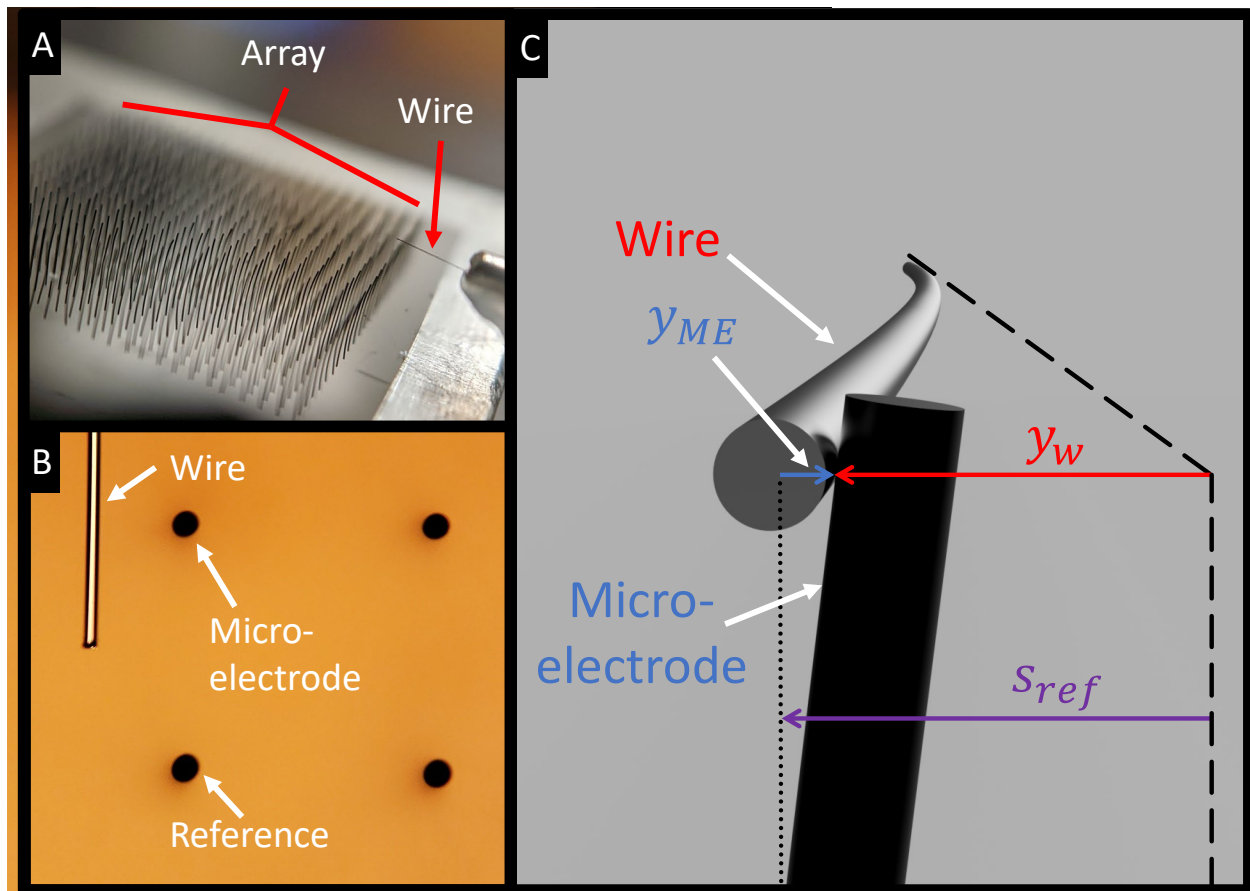


***Figure 7:*** *Overview of the dual deflection test to measure the modulus of CNT microelectrodes. A) The CNT array and the testing wire used to deflect the CNT microelectrodes. B) The top-down microscope view of the wire and probes used to measure the deflections. The reference electrode is used to measure the total distance the substrate moves, $x_{ref}$. C) A 3D representation of the wire and CNT microelectrode interaction. Distances $y_p$ and $y_w$ are the microelectrode and wire deflections, respectively. $s_{ref}$ is the total displacement of the substrate, as measured by the reference electrode in B).*

To verify the DD method, the test was performed with two segments of Stableohm 650 wire, each of known stiffness. One segment was designated as the known beam and used to measure the modulus of the other wire segment, which was designated as the unknown beam. The measured Stableohm 650 wire modulus had an error of 30% from the manufacturer's reported modulus. Error propagation through equation 9 showed that the error was dominated by the uncertainty of the wire's diameter, which had an uncertainty of 6.3%. Therefore, with the materials and methods used, the Young's moduli measured with the DD method in this work have a minimum uncertainty of 30%. Measurements of the CNT MEs were performed with the same methods as the verification test.

$$E = \left(\frac{F}{y}\right)\frac{64L^3}{3\pi d^4} \qquad\qquad 8$$

$$y_{ME} = \left(\frac{E_w}{E_{ME}}\right)\left(\frac{d_w^4 L_{ME}^3}{d_{ME}^4 L_w^3}\right)y_w \qquad\qquad 9$$

$$y_{ME} = \frac{A}{R}y_w, \qquad with\ m = \frac{A}{R}, \qquad A = \left(\frac{d_w^4 L_{ME}^3}{d_{Me}^4 L_w^3}\right), \qquad and\ R = \left(\frac{E_{ME}}{E_w}\right) \qquad 10$$

$$\left|s_{ref} - y_w\right| = y_{ME} \qquad\qquad 11$$

## 2.3   Brain-Probe Interaction FEA Model

We modeled the interaction of brain tissue with probes of varying moduli during a static micromotion deflection of 10 μm. The cylindrical probes were based on the CNT MEA by Chen *et al.* at 1000 μm long and 20 μm in diameter, but with a 10 μm radius filleted tip to avoid stress concentrations in the model. The brain was modeled as a 1500(x) x 1500(y) x 400(z) μm cuboid. The probe-brain interaction was modeled as a half-symmetry model, with half of the probe diameter embedded in the brain from the surface to a depth of 1000 μm, as seen in Figure 8. The

brain tissue was modeled as an isotropic elastic material instead of viscoelastic because our model is time independent. The brain tissue was assigned a Young's modulus of 600 Pa and was assumed to be incompressible with a Poisson's ratio of 0.48, which corresponds with other FEA modeling work [72]–[75]. The probe was modeled with a Poisson's ratio of 0.2 and moduli of 165 GPa, 1.7 GPa, 0.072 GPa, and 0.0039 GPa, which correspond to silicon, and the maximum, median, minimum measured CNT moduli, respectively. These values are found in **Table 2**.

The probe and brain tissue surfaces were tied together, i.e., a no slippage or separation constraint, with the probe as the primary surface and the brain the secondary surface. Fixed boundary conditions were applied to the lateral sides of the brain while the top face of the probe was deflected 10 μm in the positive x direction, as seen in Figure 8, to simulate a local displacement. The front and back faces were also fixed boundary conditions to preserve the integrity of the half symmetry model.

After the model converged, the maximum brain tissue strain, which is in the positive x direction (to the right) parallel to the displacement direction, was measured along two paths. The first started 10 μm from the tip tissue-probe interface to avoid edge effects and measured 620 μm in the positive x direction, i.e., parallel to the surface. The second path started 5 μm from the surface of the brain and 5 μm from the tissue-probe interface and measured 1080 μm down the

length of the probe and past the tip. The results from the first and second paths are shown in  and

, respectively.
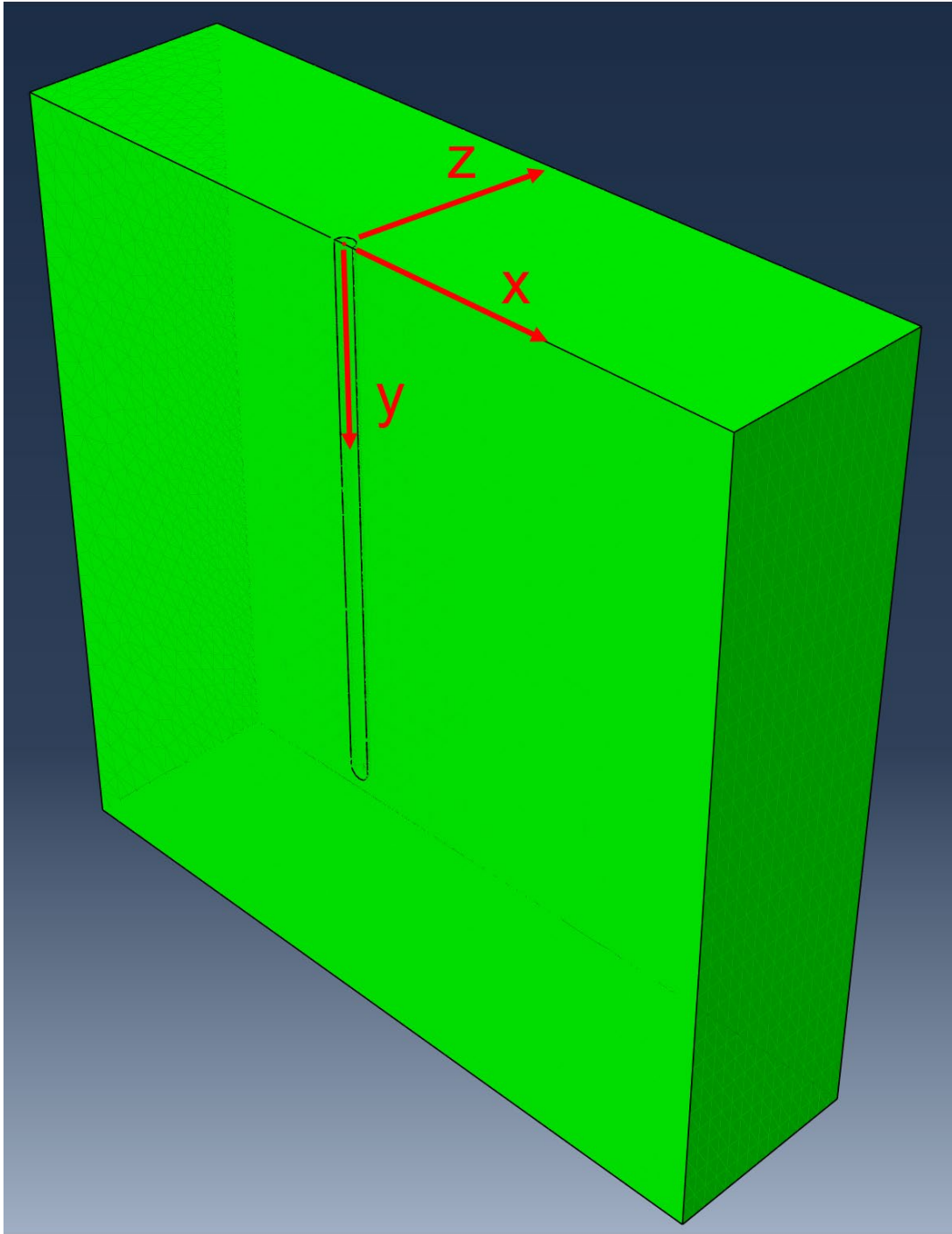


**Figure 8:** *An isometric view of the probe and brain tissue half-symmetry model used in FEA modeling. The origin is at the center of the probe at the surface of the brain.*

# 3. Results

## 3.1 Dual Deflection test
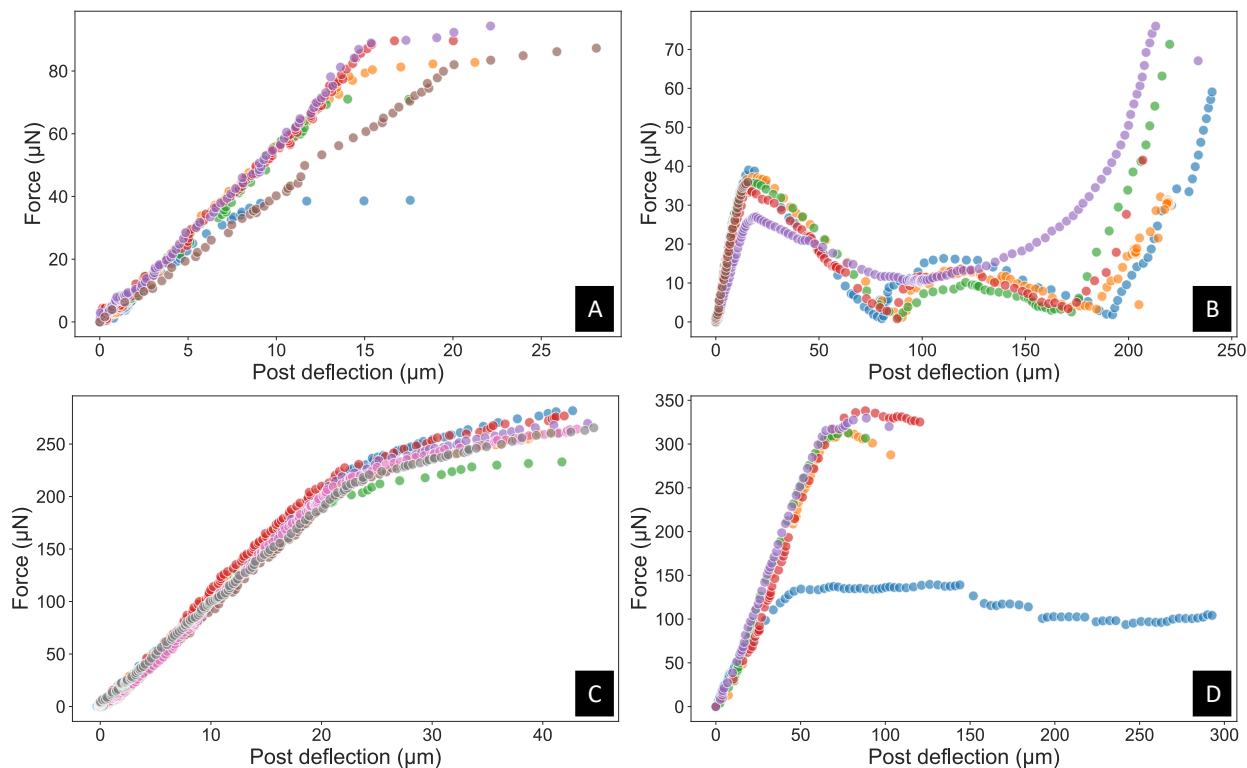


***Figure 9:*** *Raw data of the DD results showing the complete deflection data for all the CNT MEs measured on four different arrays. Each ME measured is differentiated by colored markers. A) An uninfiltrated CNT array. B) Another uninfiltrated CNT array. C) A array with 15 seconds of carbon infiltration at 900°C. D) A array with 30 seconds of carbon infiltration at 900°C.*

Over the course of this study, 64 CNT MEs were tested with the DD method. Force was applied on the ME until failure, or the ME deflected far enough that the wire slipped off. The deflection magnitude was mostly consistent per array, as seen in Figure 9, where each graph shows all the ME deflection vs wire deflection curves measured for a particular array. Wire deflection is proportional to force, which is on the scale of µN. The uninfiltrated MEs had the most varied deflection behaviors between arrays. Figure 9-A and Figure 9-B are both uninfiltrated arrays, but the MEs in array B sustained deflections ~10x larger than the MEs in array A, which only deflected ~25 µm before DD test conclusion. Array A deflection curves had

similar shapes to the deflection curves of carbon infiltrated arrays C and D, shown in Figure 9-C and Figure 9-D, respectively. Arrays A, B, and C all showed a steep linear region under initial deflection until a yield point, where the curve transitions to a zero or slightly positive sloped region until total failure. Array B also has a steep linear region during initial deflection, but after yielding, many MEs became less stiff for a large deflection region before increasing in stiffness immediately prior to DD test conclusion. Across all the arrays shown in Figure 9, the initial slopes were tightly grouped for up to 10 µm after which point, Figure 9-A and Figure 9-D show, some MEs can begin to yield significantly earlier than the others on their array. Yield points were less tightly grouped than initial slopes, even for array C, which had the tightest grouping of deflection curves out of arrays measured. Yield and ultimate strengths were not calculated due to non-linear behavior that obscured exact location of the yield and failure points. The slopes of the

initial deflection region were measured and used to calculate the modulus of the MEs. The

results are detailed later in this section and in Figure 15.
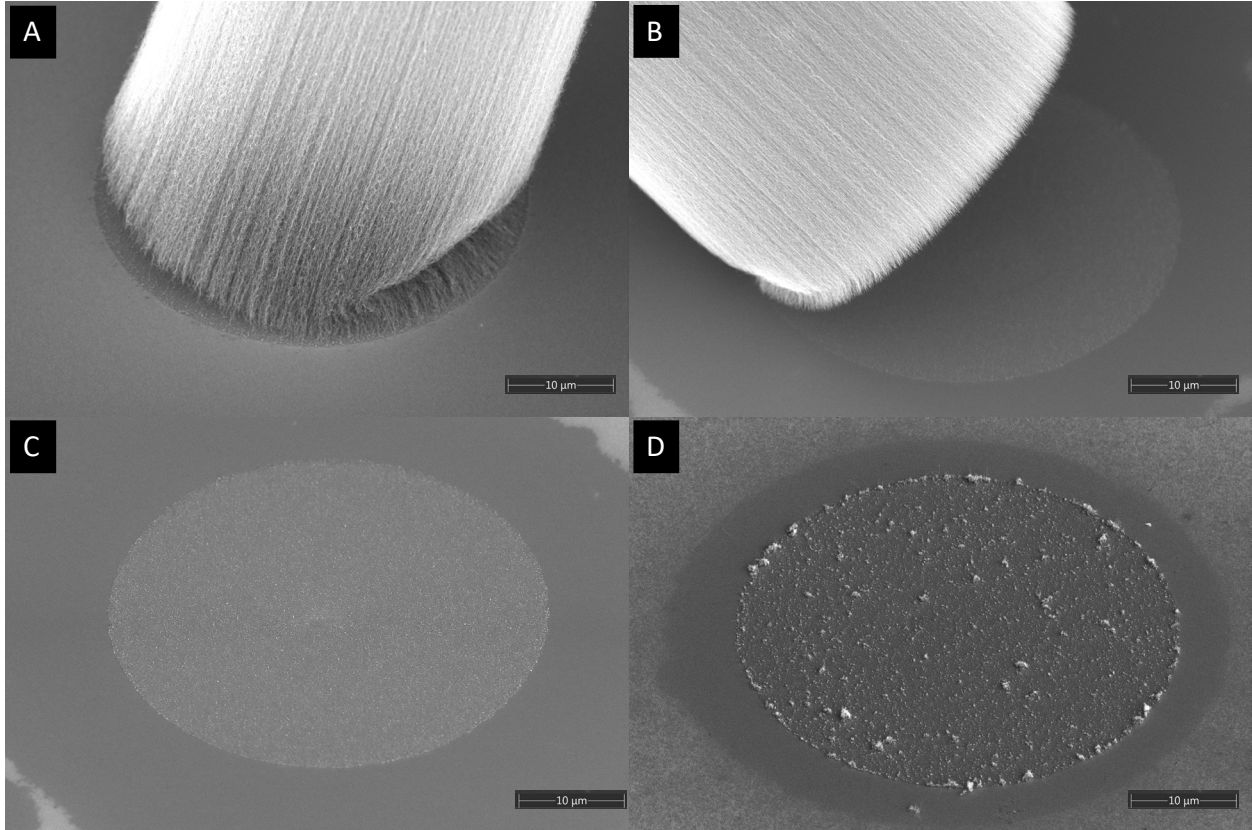


*Figure 10:* *Failure modes of uninfiltrated CNT MEs after DD tests. A) Force applied to the left side. B) Force applied to the right side. C) Short CNT "carpet" left on substate after ME removal. D) Rougher CNT "carpet" left on substrate after ME removal.*

In addition to measuring stiffness, we examined the failure modes of the CNT MEs after

DD test completion with SEM. There was a noticeable impact of carbon infiltration on failure

modes, which is shown in Figure 10-Figure 14, . Since the DD test applies a lateral force to the

MEs, stress is concentrated at the base of ME. Figure 10 shows the damage and failure modes at

the base of uninfiltrated MEs. Figure 10-A and Figure 10-B show the base of ME that received

force from the left side and right side, respectively, relative to the image. In this case, the DD test

concluded not with total failure, i.e., the removal of the ME from the surface, but by the wire

slipping off after a large deflection. The large deflection was facilitated by significant buckling

28

on the side opposite the applied force, i.e., the side under compression, and by tearing the nanotubes on the side of the force, i.e., those under tension, off the substrate. The combination of the buckling and tearing created a hinge that remained attached to the surface but permitted easy, large deflections in the direction of the initial applied force. This was verified by repeating the DD test on the ME. When force was applied in the same direction as the initial force, the ME easily deflected and did not bend the wire at all. After the wire slipped off, the ME remained tilted in the direction of the initial force. However, when the DD test applied force in the direction opposite the initial force, the ME straightened, then stiffened, providing enough force to measure deflection on the wire, before completely detaching from the substrate. Figure 10-B shows that as the ME tears off the substrate, it leaves behind a short, small, CNT residue, or "carpet", which can vary in thickness and texture depending on array. CNT carpets from two different arrays are featured in Figure 10-C and Figure 10-D and can be seen in Figure 6-A as magenta circles.
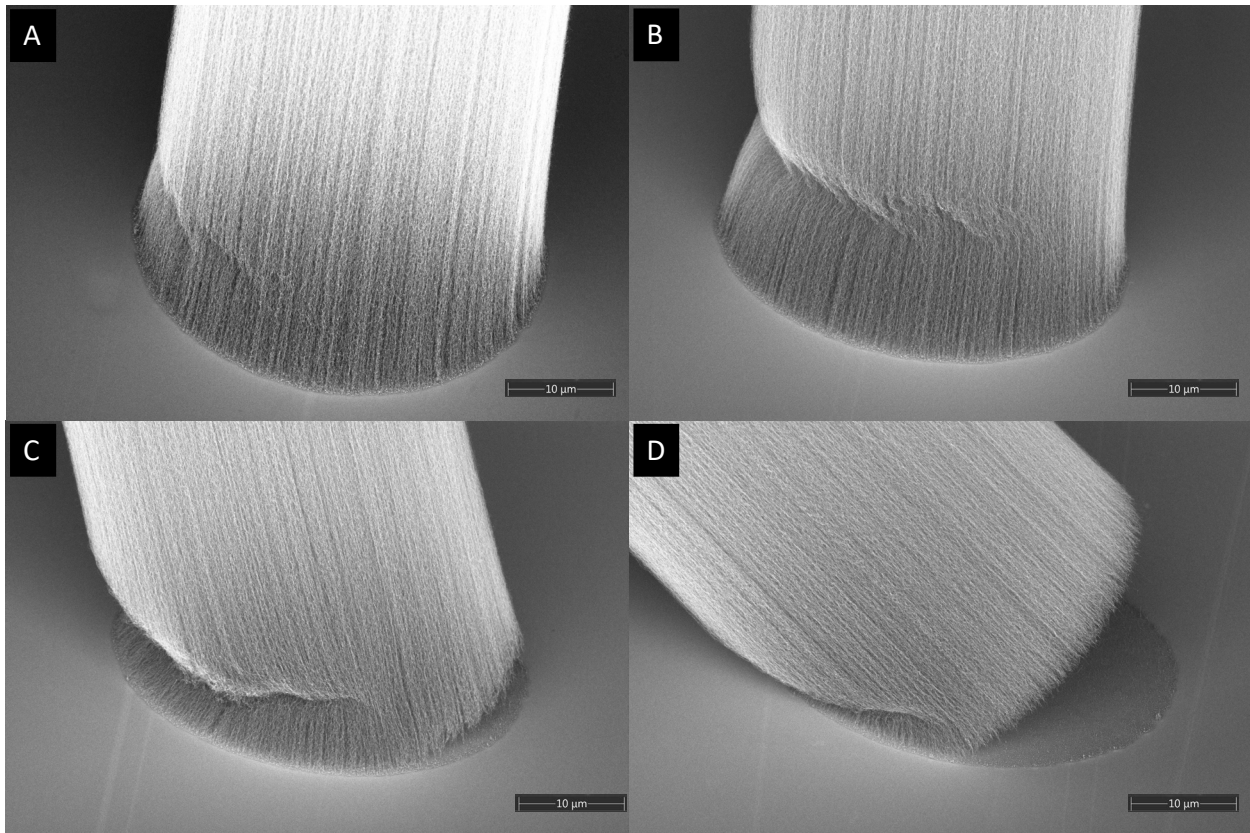
*Figure 11:* *Progression of uninfiltrated CNT MEs' failure modes with increasing deflection. A) Deflected 10-20 μm. B) Deflected 40-50 μm. C) Deflected 150-170 μm. D) Deflected 200-220 μm.*

To investigate the progression of uninfiltrated MEs' failure modes—particularly the hinging effect—we performed DD tests with different maximum deflections on 4 separate MEs on the same array. Figure 11-A shows the base of an uninfiltrated CNT ME after 10-20 μm of deflection. Deflection was increased to 40-50 μm, 150-170 μm, and 200-220 μm for parts B-D, respectively. After a 10-20 μm deflection, the ME develops a shallow buckle or kink on the side under compressive stress, about 10 μm from the surface. No tearing is evident yet. Notably, Figure 9-A and Figure 9-B show that uninfiltrated MEs can behave in a linear elastic manner during deflections of 10-20 μm. At 40-50 μm of deflection, the buckle is deeper, more pronounced, and has extended around the sides of the ME. Tearing is still not visible. However, after a 150-170 μm deflection, tearing is visible on the tensile stress side. At this point, the ME

wall below the buckle collapsed in on itself and brought the buckle much closer to the surface.

At 200-220 μm of deflection, the ME is completely detached on the tensile side and remains

hinged on the collapsed buckle, as seen by the tilted, red colored MEs in Figure 6-A.
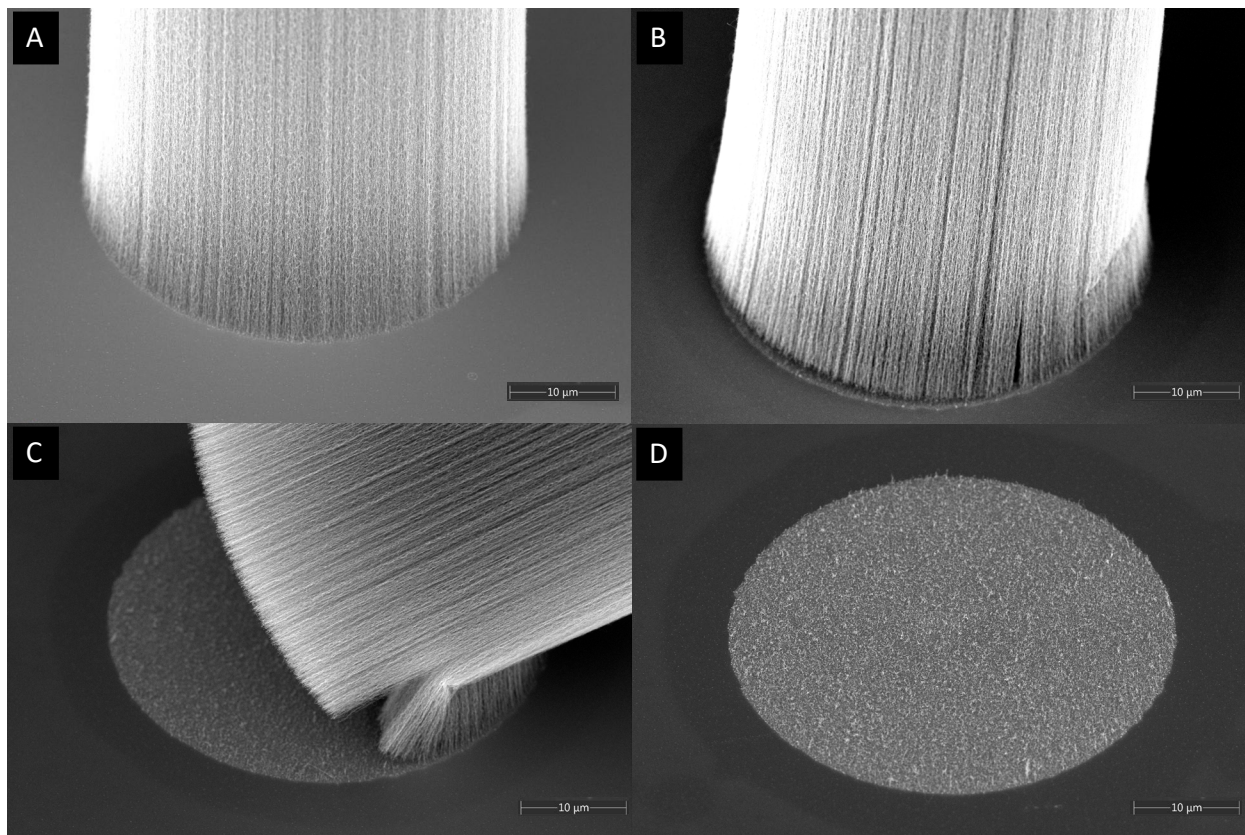


*Figure 12: Failure modes of 15 second CI-CNT MEs after DD tests. A) Force applied to the left side. No visible damage. B) Force applied to the left side. C) Force applied to the left side. D) Thick CNT "carpet" left on substrate after ME removal.*

The failure modes of CNT MEs infiltrated for 15 seconds at 900°C, are shown in Figure

12. Images A-C in Figure 12 show the bases of infiltrated MEs that underwent a complete DD

test, i.e., till the wire slipped off. Figure 12-D, shows the CNT carpet that was left behind after a

ME was torn off. In contrast to uninfiltrated MEs, some MEs with 15 seconds of infiltration did

not show any visible damage to their base after a DD test. Others developed the shallow buckles

and tears seen in other MEs (Figure 12-B, Figure 10-A, Figure 11-C). As seen in Figure 12-C,

MEs with 15 seconds of infiltration also hinged like the uninfiltrated MEs in Figure 10 and

Figure 11. However, the CNT forest under the buckle did not collapse when hinging, unlike the uninfiltrated MEs. Removal of a 15 second CI-CNT ME, also leaves behind a CNT carpet, though the CNTs in the carpet are thicker from infiltration (see Figure 6-B and C).
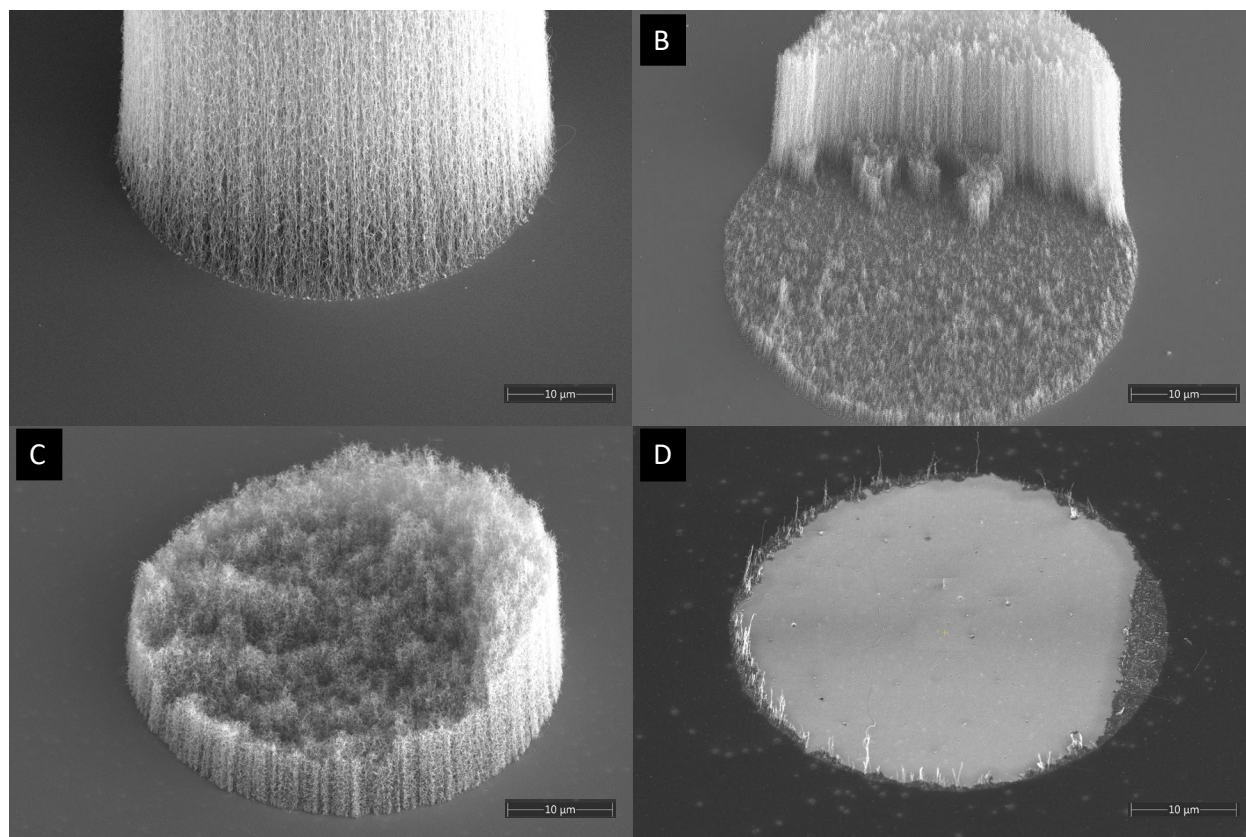


*Figure 13:* Failure modes of 30 second CI-CNT MEs after DD tests. A) Force applied to the left side. No visible damage. B) Force applied to the into the page. Half CNT "stump" and half shag CNT "carpet" left after ME failure. C) Force applied to the left side. CNT "stump" left after ME failure. D) Force applied to left side. Complete removal of CNTs and floor layer by ME failure.

Finally, the failure modes of CNT MEs infiltrated for 30 seconds at 900°C, are shown in Figure 13. The failure modes of 30 second CI-CNT MEs are unique from the other infiltration levels, though they share the same fundamental failure mechanisms. Again, some MEs appeared untouched after DD tests (Figure 13-A), but 30 second infiltrations often resulted in the ME snapping off during a DD test, leaving behind a "stump" (Figure 13-B and Figure 13-C). These stumps varied in height and area, but they were always taller on the side opposite the applied force. Some MEs left behind a combination of stump and carpet, shown in Figure 13-B, though

32

the carpet was many times taller than the carpet left behind by uninfiltrated and 15-second

infiltrated MEs. After heavier infiltrations, DD tests would result in complete removal of the ME

from the substrate without leaving a carpet behind. In these cases, as seen in Figure 13-D, the

ME would also be torn free from the carbon floor layer that deposited on the substrate during

infiltrations.
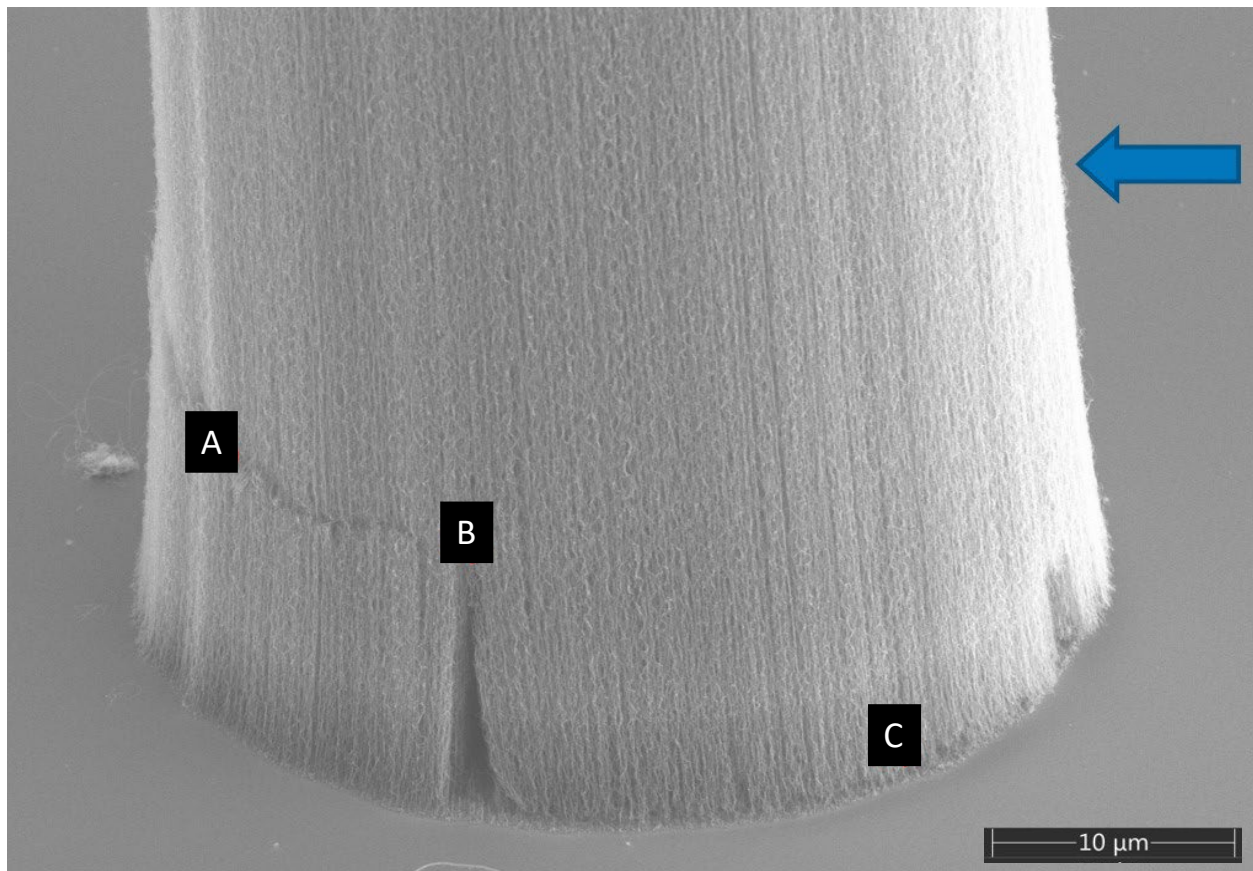


*Figure 14:* *Representative microelectrode with the most prominent features of the failure modes of CNTs MEs. The Blue arrow indicates the direction of the applied force. A) Light buckling on the side opposite the applied force. Usually, 10s of microns above the substrate. Marks the top of the "stump". B) A split where the stress switches from compressive to tensile. C) Tearing the nanotubes close to the substrate, leaving behind a carpet. Alternatively, the nanotubes rip off the surface.*

In summary of the results of CNT MEs' failure modes, Figure 14 is a representative microelectrode that neatly displays the most prominent features observed in the failure modes of CNTs MEs. While other failure modes are possible, as indicated by Figure 13-D, most microelectrodes in this study were characterized by 3 features: a shallow buckle about 10 µm above the substrate on the side opposite the applied force (Figure 14-A), a split in the forest where the stress switches from compressive to tensile (Figure 14-B), and a tensile tear on the same side as the applied force (Figure 14-C). These features were present in some form in all the microelectrodes measured, except the representative ME in Figure 13-D. The key differences between the infiltrated and uninfiltrated MEs were the sturdiness of the CNT forest below the buckle while under compression, and the height of the tear on the tensile side. For infiltrated microelectrodes, the forest under the buckle remained upright and vertically aligned and the tear tended to form higher off the surface, leading to stump formation. For uninfiltrated microelectrodes, the forest under the buckle collapsed inward and the tear formed close to the

34

surface, leading to short carpet formation.
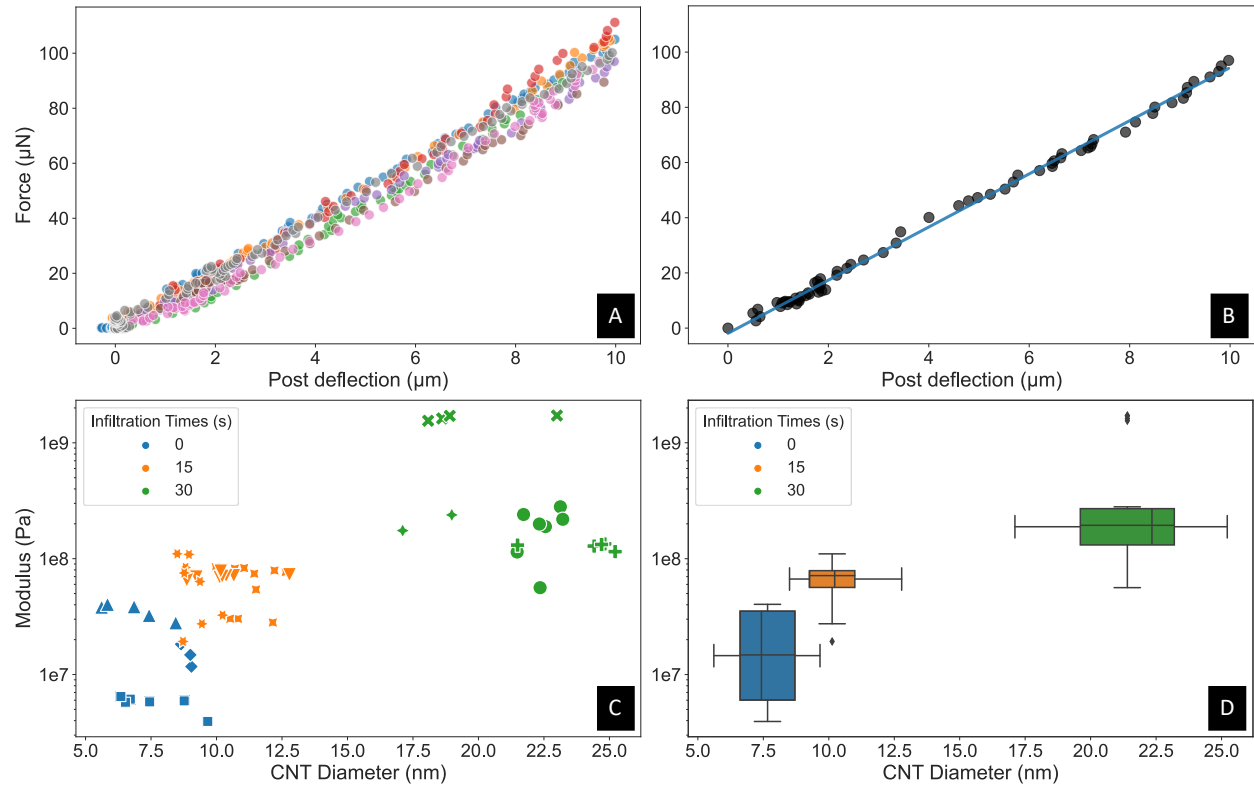


*Figure 15: Processed data from the dual deflection test. A) Force deflection data of multiple microelectrodes on a single array truncated to 10 microns of deflection. Colors differentiate microelectrodes. B) The total least squares (TLS) fit of a single post deflection. C) Modulus vs CNT diameter. The modulus is calculated with the slope of the TSL fit in B) and equation 10. Log scale of Modulus vs linear scale of CNT diameter. Each data point represents a single post, and the shapes indicate arrays. The colors indicate infiltration time. D) Dual boxplots of the Modulus vs CNT diameter grouped by infiltration time. Outliers are defined as larger than 1.5 times the inner quartile range.*

As shown in Figure 9, 64 CNT MEs were tested in this study over a large range of deflections. During large deflections, the MEs demonstrated irregular behavior and plastic deformations that are incompatible with analytic modeling to determine material properties. Also, large deflections of 100s of μm are not realistic displacements for MEs implanted in brain tissue. Micromotion induced displacements of intracortical MEs are on the scale of 10s of μm [27], [28]. Thus, considering our intended use case and to simplify the modeling, the ME deflections for determining the Young's modulus were limited to 10 μm where the MEs demonstrated Hookean behavior. We also limited our analysis to deflections that had at least 8

data points in the first 10 µm of deflection, which reduced the deflections available for analysis

from 64 to 59. The results from these 59 microelectrodes are shown in Figure 15. Figure 15-A

shows the truncated deflections from the array in Figure 9-C and Figure 15-B shows one of those

deflections and its total least squares (TLS) fit, which is used to account for errors in both the

ME deflection and the wire deflection. The slope of the TLS fit was used to calculate the

modulus of that CNT ME using equation 10. This process was repeated for all 64 deflection

curves. Figure 15-C shows the scatter of ME moduli vs CNT diameter, where the data are

grouped by shape according to array and by color according to infiltration time. Contrary to our

hypothesis, modulus data within each array and within each infiltration time group did not show

a clear trend with increasing CNT diameter. However, we grouped the data by infiltration time

and plotted dual-axis boxplots for CNT diameter and modulus (Figure 15-D), which showed

statistically that increasing infiltration time correlates positively with modulus and CNT

Diameter, thus supporting our hypothesis. We supported the uniqueness of each infiltration time

group with a 3-way Kruskal-Wallis test, which produced a p-value of 1.5e-10 when comparing

modulus and a p-value of 5.4e-12 when comparing CNT diameter. Out of the 3 infiltration times,

the 15 second and 30 second groups had modulus outliers, shown on Figure 15-D as diamond

markers. Outliers were defined as greater than 1.5 times than the interquartile range shown on

the boxplots. The 15 second infiltration time group had one low modulus outlier, while the 30

second infiltration time group had 4 high modulus outliers, which all came from the same array.

None of the average CNT diameters per microelectrode were outliers.

As expected, both CNT diameter and Young's modulus increased with infiltration time.

Excluding the outliers shown in Figure 15-D (the four green 'Xs' and one low orange 'starburst'

shown in Figure 15-C), the means and standard deviations of the CNT diameters and moduli

were 7.5 ± 1.6 nm, 10.2 ± 2.0 nm, and 22.6 ± 3.3 nm and 19.6 ± 14.5 MPa, 67.7 ± 22.7 MPa,

and 168 ± 62.3 MPa for the 0 second, 15 second, and 30 second infiltrations, respectively. The

CNT diameter results were more tightly grouped than the modulus results across the infiltration

times as evidenced by the coefficient of variance (CV). The CV is a measure of how wide a

distribution is relative to its mean and is useful to compare distributions with different units and

scales. It is calculated as,

$$CV = \frac{\sigma}{\mu} \times 100\% \qquad\qquad 12$$

where $\sigma$ is the standard deviation and $\mu$ is the mean. The modulus CV as calculated ranged from

34-74%, while the CNT diameter CV only ranged from 15-22%. The means, standard deviations,

sample size, standard error, and coefficients of variance, are shown in Table 1. A more extensive

review of these statistical parameters and their significance in this work is covered in the

discussion.

The variances of modulus and CNT diameter for each array covered a larger range than

the variances of each infiltration subset. Including outliers, the CV of the moduli ranged from

4.8% to 55% across all arrays. However, this range was dominated by the variances of the

infiltrated arrays, as the variance of the modulus only ranged from 13-16% among uninfiltrated

arrays. The spread of CNT diameter measurements was more consistent per array than the spread

of moduli. Across all arrays, the CV of CNT diameters only ranged from 12-26%. Unlike the CV

of the moduli, the largest range of variances of CNT diameters was among the uninfiltrated

arrays, which ranged from 15-26%. Notably, the one array that produced the four modulus

outliers in the 30 second group—marked in Figure 15-C with green 'X's—had the most tightly

grouped modulus results, with the highest mean of 1.65 GPa and the lowest CV at 4.8%.

*Table 1: Statistical quantification of microelectrodes' moduli and CNT diameters, excluding outliers greater than 1.5 times the interquartile range. MEs were grouped by infiltration time for quantification.*

| Infiltration time | 0 seconds | 15 seconds | 30 seconds |
| --- | --- | --- | --- |
| Number of MEs measured | 15 | 25 | 14 |
| Modulus: Mean | 19.6 MPa | 67.7 MPa | 168 MPa |
| Modulus: Standard Dev (SD) | 14.5 MPa | 22.7 MPa | 62.3 MPa |
| Modulus: CV | 74% | 34% | 37% |
| Modulus: Standard Error (SEM) | 3.76 MPa | 4.55 MPa | 16.7 MPa |
| Number of CNTs measured | 322 | 784 | 338 |
| CNT Diameter: Mean | 7.5 nm | 10.2 nm | 22.6 nm |
| CNT Diameter: Standard Dev (SD) | 1.6 nm | 2.0 nm | 3.3 nm |
| CNT Diameter: CV | 22% | 20% | 15% |
| CNT Diameter: Standard Error (SEM) | 0.09 nm | 0.07 nm | 0.20 nm |

## 3.2   FEA Model

To determine if probe tip strain could be reduced using CNT MEs, FEA modeling was performed using the max (1.7 GPa), median (72 MPa), and minimum (3.9 MPa) CNT moduli we measured, as well as the modulus of silicon (165 GPa) for comparison (Figure 16). The probe geometry used in the simulation was the high aspect ratio CNT probe geometry reported by Chen et al., i.e. 1000 μm in length and 20 μm in diameter, but with a rounded tip [42]. Figure 16 (c-f) shows the heat maps of the x direction strain for all four probe moduli. Unlike the two higher moduli probes, visible bending can be seen in lower moduli probes' heat maps (Figure 16 e-f). Two paths of interest were measured on each heat map and the results are shown in the graphs in Figure 16 (a-b). The paths are represented by the dashed red arrow on the model-sketch-insert in each graph. The graph in Figure 16 (a) shows strain at the probe tissue interface along the entire vertical length of the probe. Each probe fulcrumed in the brain, indicated by the point where the lines cross zero strain, i.e. where strain transitions from compression to tension. Black dots were added to the graph to mark the point of highest strain after fulcruming. Despite being ~100 times less stiff, the highest CNT modulus probe induces strain almost identical to that induced by the

Si probe. Both fulcrum near the same point and both show a spike in brain tissue strain near their tips. In contrast, the 72 MPa and 3.9 MPa CNT probes fulcrum early, have low peak strains after fulcruming, and drop to near-zero strain at the tip. Figure 16 (b) examines how strain drops off laterally from the probe tip. The zero-strain region in the middle of the plot is where the measurement line passes through the probe tip. The Si probe induces a peak tip strain ~1.3x greater than the peak tip strain induced by the 1.7 GPa CNT probe. On the other extreme, the Si probe is ~42,307x stiffer than the most flexible CNT probe and induces a peak tip strain ~1000x greater. In the upper right-hand corner of Figure 16 (b), an inset graph with a strain scale 250 times smaller shows the strain spikes for the 72 MPa and 3.9 MPa. A base level of strain is maintained for each low modulus probe over the entire measurement path, i.e., ~460 microns in each direction from the probe tip. Interestingly, despite being ~18x stiffer, the 72 MPa probe only induces a strain ~3x greater than the 3.9 MPa probe.

*Table 2: Comparison of the CNT moduli and the strain their probes induced in brain tissue relative to a silicon probe of the same geometry.*

| Probe | Modulus | $E_{CNT}/E_{Si}$ | $\epsilon_{tip,CNT}/\epsilon_{tip,Si}$ |
|---|---|---|---|
| **Silicon** | 165 GPa | - | - |
| **CNT Maximum** | 1.7 GPa | 1e-2 | 0.77 |
| **CNT Median** | 72 MPa | 4e-4 | 3.3e-3 |
| **CNT Minimum** | 3.9 MPa | 2e-5 | 9.9e-4 |
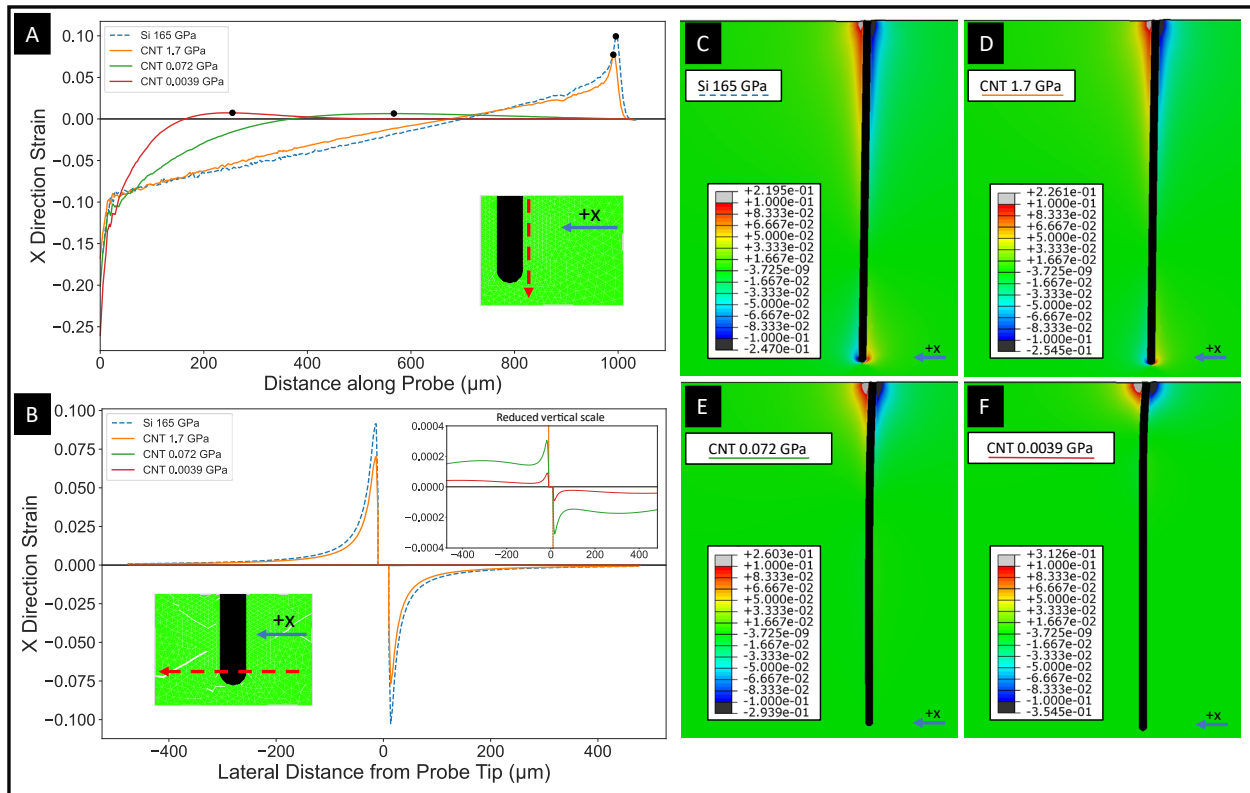
*Figure 16:* *FEA model of brain tissue strain when the top of the ME is deflected 5 ums. Strain and deflection are both in the X direction, as indicated by the blue arrows. The maximum, minimum, and median moduli of CNT MEs recorded in this study and the modulus of silicon are used. (A-B) are measurement profiles of the strain heatmaps shown in (C-F). A) the strain profile measured parallel to the probe on the right side as indicated by the red dashed arrow. The black dots mark the point of highest strain after fulcruming (crossing zero). B) The strain profile measured perpendicular to the ME and 10 microns above the tip, as indicated by the red dashed arrow. The segment of zero strain near 0 is where the measurement line passes through the ME. To visualize the small strains of the lower two moduli, a zoomed in graph is shown in the upper right-hand corner. The heat maps of brain strain with deflected, implanted probes are show with C) a 165 GPa silicon probe, D) a 1.7 GPa CNT probe, E) a 0.072 GPa (72 MPa) CNT probe, and F) a 0.0039 GPa (3.9 MPa) CNT probe.*

# 4. Discussion

This work sought to examine the fundamental mechanical properties of carbon nanotube microelectrode arrays in the context of their potential application as intracortical neural probes. Thus, the results can be examined and discussed in two contexts: a characterization of a unique MEMS material for general use, and a characterization a potential neural probe platform. The neural probe use case was useful in guiding our experimental design, such as motivating and justifying truncating deflections to the scale of micromotion in the brain but could also prove burdensome with its bevy of requirements. It is useful to first examine these results as simply a

study of materials, without the neural probe application context, to avoid getting bogged down by the engineering requirements of intracortical arrays. After discussing the material and methods related implications and questions, the neural probe context will provide an exciting motivation that highlights particular results and illuminates future work.

## 4.1    Characterization of CNT Microelectrodes

Our results show that with up to 30 seconds of carbon infiltration at 900°C, CNT structures with moduli ranging from single MPa to single GPa can be produced. Thus, we can produce high-aspect ratio, pure carbon structures with moduli comparable to polyimide all the way down to crosslinked PDMS [76]. The effect of increasing infiltration time on CNT diameter and CNT ME modulus is strongly demonstrated by the data in Figure 15-D. Our initial hypothesis was that increasing infiltration time would increase the CNT diameter which would in turn increase the modulus by locking the nanotubes together as they grow thicker. We anticipated that measuring the nanotube diameters would serve as a quantification of infiltration levels and a predictor of modulus. As evidenced by the boxplots in Figure 15-D, infiltration time could be used to determine the range of nanotube diameters and the range of potential moduli. However, within each array or each infiltration group, CNT diameter cannot be used to predict modulus. There are arrays whose moduli trend upward with increasing CNT diameter and arrays whose moduli trend downward or just stay the same. The most notable of theses is the one outlier array marked in Figure 15-C with green 'X's. Despite consistently measuring a modulus ~10x the next highest array average, the CNT diameter of this array measured ~3 nm less than the same array. Thus, in an infiltration group there is evidence of no modulus dependency on CNT diameter. There is also no apparent correlation between MEs on the same array. The CNT diameter increased by ~5 nm, but modulus remained roughly constant. These results are counter intuitive and contrary to our

initial hypothesis, which holds true on the scale of infiltration groups. It is possible that there are uncontrolled variables impacting the modulus of a CNT forest, such as high density that results in a base level of locking together the CNTs with infiltration and serves as a point of diminishing returns with infiltration until the forest filled. Another possibility is that measurements of CNTs are not representative of the array. Since CNT diameters are measured with high magnification SEM images like in Figure 6-B and C, we are limited a very small area to make our CNT diameter estimate. It is possible that the area we measured does not represent the average CNT diameter of the array well, leading to the irregular CNT diameter vs Modulus trends we see in Figure 15-D, though that is not supported by the statistics in Table 1. Before discussing those results, we will briefly review how to interpret each statistical value with respect to these results.

Standard deviation (SD) shows the variation in a data set, which in this work is the modulus or CNT diameter of either a array or a subset of arrays grouped by infiltration time. The coefficient of variance is a unitless ratio of the standard deviation or standard error divided by the mean and is useful to compare variances between data sets have means of very different magnitudes or different units. The moduli of CNT MEs vary on a log scale, such that in this work there are arrays with mean moduli separated by almost three orders of magnitude. As such, CVs are used to compare modulus variations between arrays and infiltration time groups. It is also useful to compare variations in CNT diameter and modulus to better understand the relationship between the two parameters, i.e., does a large variance in CNT Diameter correlate with a large variance in modulus? The standard error used to indicate how much a sample's mean may vary from the population mean and is inversely proportional to sample size. In this work, standard error is used to estimate how much the means of CNT diameters and ME moduli of each infiltration time group differ from the mean of the total population of CNT MEs grown

42

and infiltrated with the same recipe. In other words, if I were to produce and measure another batch of CNT ME arrays with 15 seconds of infiltration, how close would the mean modulus be to 67.2 MPa and the mean CNT diameter be to 10.2 nm? Standard error can help quantify what is the variation of a specific infiltration recipe's output. However, due to the relatively small sample sizes per infiltration group, the uncontrolled variables in fabrication and measurement might have an outsized impact on the modulus of arrays produced for this work. In converse, we measured over 1800 CNT diameters, resulting in standard errors less than a nanometer, indicating the diameter means are well representative of the CNT diameter populations per infiltration time.

A comparison of our results with the previous work by Laughlin *et al.* and Hanna *et al.* (section 1.4.1) demonstrate that the modulus of CI-CNT structures is largely dependent on orientation and infiltration regime. Laughlin *et al.* reported a transverse Young's modulus ranging from 60 kPa to 7000 kPa (7MPa) for uninfiltrated structures and structures with 5 minutes of infiltration, respectively. Hanna *et al.* reported a transverse Young's modulus ranging from 8.6-4.1 GPa and 7.4-15.7 GPa with infiltration times of 30 and 120 minutes, respectively. They also reported a parallel Young's modulus of 11 GPa after 30 min of infiltration. Parallel and Transverse refer to the direction of the stress relative to the CNT alignment. We reported parallel Young's moduli ranging from 3.9 MPa with no infiltration, to 1.7 GPa with 30 seconds of infiltration. Per Laughlin *et al.* results, the modulus of CNT structures seems to depend largely on the anisotropic alignment CNT forests relative to the applied stress, especially at low infiltration levels. Thus, the only data comparable to ours is the 11 GPa parallel Young's modulus reported by Hanna *et al.* Our structures were only infiltrated for 30 seconds, compared to 60x infiltration Hanna *et al.* used. A consistent feature of Hanna *et al.*, Laughlin *et al.,* and our

own work is that increasing carbon infiltration time increases modulus. This relationship holds when comparing our results with the 11 GPa parallel Young's modulus from Hanna *et al.*, indicating that our results agree with existing literature.

Though they are not used in the modulus calculations, the large deflections recorded during the DD tests reveal some interesting behaviors of CNT MEs. First, the ultimate or yield strength can be independent of modulus and vary between MEs on the same array. Some MEs, as seen in Figure 9-B and Figure 9-D, exhibit tougher behavior than other MEs on the same array, deflecting for hundreds of microns before total failure. Notably the uninfiltrated MEs in Figure 9-B, exhibit deflection curves that are consistent with traditional force deflection curves of other elastic materials. The correlation between these behaviors and the failure modes shown in Figure 10 through Figure 14 are not known. Surprisingly, the uninfiltrated MEs begin to plastically buckle after just 10 to 20 microns of deflection, despite 10 to 20 microns being within the consistent linear elastic region of the deflection curves. The most notable difference between the infiltration levels is that infiltrated nanotubes below the buckle can withstand the compressive force during deflection and remain vertically aligned, while the uninfiltrated nanotube forests collapse during bending. Occasionally, infiltrated MEs will hinge on the buckle then snap back to a near vertical position. But because half of the ME base tore off in tension and the buckle is already formed, the ME easily deflects in the direction of the original deflection, but it is stiff in the opposite direction. This could have implications for directional sensors and one-way micro gates. This failure regime could be used to estimate surface adhesion strength of the carbon nanotubes as a function of infiltration.

A notable achievement of this work is the development and validation of the dual deflection test method for vertical cantilevers, especially those with anisotropic mechanical

characteristics. Like Hanna *et al.* and Laughlin *et al.,* most mechanical characterization studies of CNT explore the high moduli regime with highly infiltrated forests, composites, or yarns [77]–[79]. Those that do explore the lower moduli regimes test the structures under compression or nanoindentation [80]–[82]. There is no prior literature exploring the lower limit of the parallel Young's modulus of CNT structures, likely due to the difficulty in handling and testing such fragile structures. The DD test overcomes this challenge since the cantilevers do not need to be removed from the substrate for 3-point bending tests as Hanna *et al.* did. Testing arrays as fabricated reduces the handling errors of fragile arrays and enables high throughput. The DD method proved to be compatible with a wide range of stiffnesses, simply by changing the length or material of the testing wire. The DD method is especially useful for testing MEAs in the same form factor intended for use, allowing for evaluation of substrate adhesion and performance after deflection, something that traditional 3-point bending does not facilitate. A limiting factor of the current DD method is that the stiffness of the wire is not measured directly but calculated with elastic modulus and geometry. The small diameter of the wire, 20 µm, is difficult to measure accurately and the uncertainty in that measurement is magnified when calculating stiffness since the diameter term is raised to the fourth power (see equation 8).

## 4.2   FEA Model and CNT neural probes

Examining the performance of the CNT MEs and the DD test in the context of neural probe applications illuminates additional benefits of both. The DD test is well suited to simulate tangential micromotions in brain tissue on microelectrode arrays. The DD setup can perform controlled deflection of microelectrodes on the scale of a few microns and can be scaled to fit dense array dimensions by simply swapping out the testing wire with another material of known stiffness, like a carbon fiber, that fits the scale of the high-density array. The range of CNT

moduli measured in this work is significant for neuro implants. The high end of CNT moduli in this work is comparable of polyimide and parylene C, both significant materials in neural probe fabrication. Polyimide has been used to make flexible neural probes that seek to solve the biocompatibility issue induced by compliance mismatch with longer geometries and a lower modulus than silicon. Being able to achieve the same modulus as polyimide opens up the possibility of future studies comparing biocompatibility of polyimide arrays versus CNT arrays. Remarkably, the 1.7 GPa modulus was the highest of our range, with the MEs able to go as low as 3.9 MPa. This is significant because at the single megapascal range CNT probes can start to compete with ultra soft polymer arrays, which are usually more planar in shape since the soft polymers are difficult to fabricate in high-aspect ratios. CNTs possess a unique advantage on this front, as they are capable of being fabricated in the same high aspect ratio design regardless of modulus.

To determine which range of CNT modulus values would be most useful for a brain probe, we used FEA to model probe deflection in brain tissue.  indicates that a 3.9 MPa probe, which achievable with our CNT MEs, produces the greatest reduction in brain tissue strain during micromotion. However, the 3.9 MPa probe is likely too soft to insert into the brain without collapsing and would thus require assisted insertion, like a stiff shuttle or hard coating. The next smallest modulus—72 MPa—produced results similar to the 3.9 MPa probe, indicating that the principal area of interest is around the 72 MPa probes, as they would not greatly increase strain and may be stiff enough for unassisted insertion.

Remarkably, for the dimensions we were using in our model, the 1.7 GPa and the 165 GPa behaved similarly. This is significant because 1.7 GPa is close to that of polyamide, and the results imply simply lowering the modulus from that of silicon to that of polyimide is not enough

to alleviate the strain on brain tissue. To have a significant reduction in brain strain, polyimide probes also need to use reduced geometry. Thus, compete with polyimide, highly infiltrated CNT probes need to be reduced in diameter and increased in length, beyond the dimensions used in our FEA model.

## 4.3    Conclusions

We approached this work with an application driven question about the fundamental mechanical properties of CNT microelectrodes: could we make and measure high-aspect CNT electrodes with moduli in the range that would significantly reduce brain tissue strain compared to silicon probes? To answer this question, we grew CNT MEAs with 3 levels of carbon infiltration, designed and validated a novel microelectrode testing method, and modeled the results with an FEA model to simulate brain tissue strain. We successfully produced and tested 64 CNT electrodes that covered a range of 3.9 MPa to 1.7 GPa. We concluded that increasing infiltration time would increase CNT diameter and modulus, but the relationship between CNT diameter and modulus could not be determined. We modeled that range and compared the strain induced in brain tissue by each modulus, including silicon to represent the UEA. The model indicated that probes in the range of 3.9 MPa significantly reduced strain at the probe tip. Thus, we concluded that uninfiltrated CNT probes are the most likely candidates to significantly reduce brain tissue strain in a real-world application.

# 5.    Future work

The driving motivation for future research is to advance the CNT MEA technology to the point of viability and eventually clinical application. Improvements to the material science study of this work would be an important first step toward CNT MEA viability. First, improvement could be made to the DD test to improve the sensitivity and accuracy of the system. Machine

controlled micrometers could control the speed of deflection to be the same on every ME, removing possible variability in the modulus measurements. A significant improvement would be to measure the stiffness of the wire directly, removing the uncertainty stemming from the wire diameter. This might be achieved with a nanoindenter, or by securing a very small weight on the end and measuring the deflection. Improvements in quantifying infiltration via weight with a precision scale could improve modulus tuning capacities and replace tedious CNT diameter measurements. Besides improvement to the measuring and testing methods, ways to lower the minimum uninfiltrated CNT probe modulus could be investigated. This would entail a fractional factorial study examining the effects of growth parameters like iron thickness, temperature, gas flow rate, and gas composition. The most parameter with the highest likely impact is iron thickness and would need to be controlled and measured accurately to provide meaningful insight.

A simple improvement to this study is to modify the FEA model to include narrower ME geometries matching the high-aspect electrodes produced by Chen *et al.* This would reduce the stiffness of the MEs and better inform researchers what is the maximum modulus that can be achieved while still significantly reducing the brain tissue strain. The model could also be modified to granularly examine the range between 3.9 MPa and 72 MPa and find what is the maximum modulus that can be achieved while still significantly reducing the brain tissue strain.

There are many considerations and challenges that must be addressed to bring the CNT MEA closer to viability, but the two most important are how well can the CNT MEA endure the *in vivo* environment and how will the body respond to the CNT probes, i.e., robustness and biocompatibility. There are numerous experiments that can address the questions, but I will list a few that I believe are the most feasible and productive. For robustness, there are three

experiments that will expose the CNT MEA to specific stresses it will need to endure. The first is the repetition of the DD test while the array is submerged in saline, which will require minor modifications to the DD setup. This will simulate the *in vivo* conditions and provide a better understanding of the effective modulus during chronic implantation. The second experiment is to insert the CNT MEA in ager gel to simulate the compressive forces the array would experience during implantation. This would provide critical information about whether the array can withstand implantation in its current iteration. If the array fails implantation, then methods to strengthen it, either temporarily or permanently, must be explored as soon as possible so the DD test and all other tests can be completed with the most recent model and accurate mechanical data can be recorded. Third, is an accelerated aging test. This test simulates the body's corrosive environment at an accelerated rate and is used to evaluate the resilience of the material and its encapsulations layers. This test would provide insight into the chemical stability of CNT probes in the presence of oxygen radicals and provide a platform for testing different encapsulation layers.

In addition to robustness tests, biocompatibility tests are extremely important. Due to contradictory reports on CNT toxicity, regulators at the FDA and abroad will require thorough evidence supporting the safety of implanting the CNT MEA in a human brain. A histology study with implantations of CNT probes with varying infiltration time into rat brains will allow researchers to evaluate the severity of the foreign body response to CNT probes over a series of infiltrations. Beyond the advancement of CNT MEAs, this study would be the first controlled study that deliberately examines the effect of modulus on foreign body response severity, while controlling for probe size, shape, and chemical composition.

CNT MEAs are an exciting technology that could become a very successful intracortical array. This work is one of the first in addressing concerns to make that possible. I hope it is the first of many.

# Bibliography

[1] J. A. George *et al.*, "Long-term performance of Utah slanted electrode arrays and intramuscular electromyographic leads implanted chronically in human arm nerves and muscles," *J. Neural Eng.*, vol. 17, no. 5, p. 056042, Oct. 2020, doi: 10.1088/1741-2552/abc025.

[2] W. Yang, Y. Gong, and W. Li, "A Review: Electrode and Packaging Materials for Neurophysiology Recording Implants," *Front. Bioeng. Biotechnol.*, vol. 8, 2021, Accessed: Jan. 20, 2023. [Online]. Available: https://www.frontiersin.org/articles/10.3389/fbioe.2020.622923

[3] C. Sponheim *et al.*, "Longevity and reliability of chronic unit recordings using the Utah, intracortical multi-electrode arrays," *J. Neural Eng.*, vol. 18, no. 6, p. 066044, Dec. 2021, doi: 10.1088/1741-2552/ac3eaf.

[4] A. Joshi-Imre *et al.*, "Chronic recording and electrochemical performance of amorphous silicon carbide-coated Utah electrode arrays implanted in rat motor cortex," *J. Neural Eng.*, vol. 16, no. 4, p. 046006, Aug. 2019, doi: 10.1088/1741-2552/ab1bc8.

[5] J. Krüger, F. Caruana, R. Dalla Volta, and G. Rizzolatti, "Seven years of recording from monkey cortex with a chronically implanted multiple microelectrode," *Front. Neuroengineering*, vol. 3, 2010, doi: 10.3389/fneng.2010.00006.

[6] J.-W. Hong, C. Yoon, K. Jo, J. H. Won, and S. Park, "Recent advances in recording and modulation technologies for next-generation neural interfaces," *iScience*, vol. 24, no. 12, p. 103550, Dec. 2021, doi: 10.1016/j.isci.2021.103550.

[7] E. R. Kandel, J. Koester, S. Mack, and S. Siegelbaum, *Principles of Neural Science*, 6th ed. McGraw-Hill Professional, 2021.

[8] D. Moran, "Evolution of brain–computer interface: action potentials, local field potentials and electrocorticograms," *Curr. Opin. Neurobiol.*, vol. 20, no. 6, pp. 741–745, Dec. 2010, doi: 10.1016/j.conb.2010.09.010.

[9] T. D. Y. Kozai *et al.*, "Comprehensive chronic laminar single-unit, multi-unit, and local field potential recording performance with planar single shank electrode arrays," *J. Neurosci. Methods*, vol. 242, pp. 15–40, Mar. 2015, doi: 10.1016/j.jneumeth.2014.12.010.

[10] P. Takmakov, K. Ruda, K. S. Phillips, I. S. Isayeva, V. Krauthamer, and C. G. Welle, "Rapid evaluation of the durability of cortical neural implants using accelerated aging with reactive oxygen species," *J. Neural Eng.*, vol. 12, no. 2, p. 026003, Jan. 2015, doi: 10.1088/1741-2560/12/2/026003.

[11] R. Caldwell, M. G. Street, R. Sharma, P. Takmakov, B. Baker, and L. Rieth, "Characterization of Parylene-C degradation mechanisms: In vitro reactive accelerated aging model compared to multiyear in vivo implantation," *Biomaterials*, vol. 232, p. 119731, Feb. 2020, doi: 10.1016/j.biomaterials.2019.119731.

[12] A. Schander, J. M. Gancz, M. Tintelott, and W. Lang, "Towards Long-Term Stable Polyimide-Based Flexible Electrical Insulation for Chronically Implanted Neural Electrodes," *Micromachines*, vol. 12, no. 11, Art. no. 11, Nov. 2021, doi: 10.3390/mi12111279.

[13] N. Eliaz, "Corrosion of Metallic Biomaterials: A Review," *Materials*, vol. 12, no. 3, Art. no. 3, Jan. 2019, doi: 10.3390/ma12030407.

[14] P.-A. Mouthuy *et al.*, "Biocompatibility of implantable materials: An oxidative stress viewpoint," *Biomaterials*, vol. 109, pp. 55–68, Dec. 2016, doi: 10.1016/j.biomaterials.2016.09.010.

[15] V. S. Polikov, P. A. Tresco, and W. M. Reichert, "Response of brain tissue to chronically implanted neural electrodes," *J. Neurosci. Methods*, vol. 148, no. 1, pp. 1–18, Oct. 2005, doi: 10.1016/j.jneumeth.2005.08.015.

[16] D. Zhang *et al.*, "Dealing with the Foreign-Body Response to Implanted Biomaterials: Strategies and Applications of New Materials," *Adv. Funct. Mater.*, vol. 31, no. 6, p. 2007226, 2021, doi: 10.1002/adfm.202007226.

[17] F. Lotti, F. Ranieri, G. Vadalà, L. Zollo, and G. Di Pino, "Invasive Intraneural Interfaces: Foreign Body Reaction Issues," *Front. Neurosci.*, vol. 11, 2017, doi: 10.3389/fnins.2017.00497.

[18] N. Wu, S. Wan, S. Su, H. Huang, G. Dou, and L. Sun, "Electrode materials for brain–machine interface: A review," *InfoMat*, vol. 3, no. 11, pp. 1174–1194, 2021, doi: 10.1002/inf2.12234.

[19] G. Kook, S. W. Lee, H. C. Lee, I.-J. Cho, and H. J. Lee, "Neural Probes for Chronic Applications," *Micromachines*, vol. 7, no. 10, Oct. 2016, doi: 10.3390/mi7100179.

[20] A. M. Stiller *et al.*, "A Meta-Analysis of Intracortical Device Stiffness and Its Correlation with Histological Outcomes," *Micromachines*, vol. 9, no. 9, Art. no. 9, Sep. 2018, doi: 10.3390/mi9090443.

[21] M. Leber *et al.*, "Advances in Penetrating Multichannel Microelectrodes Based on the Utah Array Platform," in *Neural Interface: Frontiers and Applications*, X. Zheng, Ed., in Advances in Experimental Medicine and Biology. , Singapore: Springer, 2019, pp. 1–40. doi: 10.1007/978-981-13-2050-7_1.

[22] R. A. Normann and E. Fernandez, "Clinical applications of penetrating neural interfaces and Utah Electrode Array technologies," *J. Neural Eng.*, vol. 13, no. 6, p. 061003, Oct. 2016, doi: 10.1088/1741-2560/13/6/061003.

[23] R. A. Normann, E. M. Maynard, K. S. Guillory, and D. J. Warren, "Cortical implants for the blind," *IEEE Spectr.*, vol. 33, no. 5, pp. 54–59, May 1996, doi: 10.1109/6.490057.

[24] P. J. Rousche and R. A. Normann, "Chronic recording capability of the Utah Intracortical Electrode Array in cat sensory cortex," *J. Neurosci. Methods*, vol. 82, no. 1, pp. 1–15, Jul. 1998, doi: 10.1016/S0165-0270(98)00031-4.

[25] R. A. Normann, B. A. Greger, P. House, S. F. Romero, F. Pelayo, and E. Fernandez, "Toward the development of a cortically based visual neuroprosthesis," *J. Neural Eng.*, vol. 6, no. 3, p. 035001, Jun. 2009, doi: 10.1088/1741-2560/6/3/035001.

[26] "510(k) Premarket Notification." Accessed: Jul. 06, 2022. [Online]. Available: https://www.accessdata.fda.gov/scripts/cdrh/cfdocs/cfpmn/pmn.cfm?ID=K110010

[27] H. Lee, R. V. Bellamkonda, W. Sun, and M. E. Levenston, "Biomechanical analysis of silicon microelectrode-induced strain in the brain," *J. Neural Eng.*, vol. 2, no. 4, pp. 81–89, Sep. 2005, doi: 10.1088/1741-2560/2/4/003.

[28] A. Gilletti and J. Muthuswamy, "Brain micromotion around implants in the rodent somatosensory cortex," *J. Neural Eng.*, vol. 3, no. 3, pp. 189–195, Sep. 2006, doi: 10.1088/1741-2560/3/3/001.

[29] R. Biran, D. C. Martin, and P. A. Tresco, "The brain tissue response to implanted silicon microelectrode arrays is increased when the device is tethered to the skull," *J. Biomed. Mater. Res. A*, vol. 82A, no. 1, pp. 169–178, 2007, doi: 10.1002/jbm.a.31138.

[30] P. Moshayedi *et al.*, "The relationship between glial cell mechanosensitivity and foreign body reactions in the central nervous system," *Biomaterials*, vol. 35, no. 13, pp. 3919–3925, Apr. 2014, doi: 10.1016/j.biomaterials.2014.01.038.

[31] S. Y. Mian, J. R. Honey, A. Carnicer-Lombarte, and D. G. Barone, "Large Animal Studies to Reduce the Foreign Body Reaction in Brain–Computer Interfaces: A Systematic Review," *Biosensors*, vol. 11, no. 8, Art. no. 8, Aug. 2021, doi: 10.3390/bios11080275.

[32] N. Sharafkhani *et al.*, "Neural tissue-microelectrode interaction: Brain micromotion, electrical impedance, and flexible microelectrode insertion," *J. Neurosci. Methods*, vol. 365, p. 109388, Jan. 2022, doi: 10.1016/j.jneumeth.2021.109388.

[33] L. E. Bilston, "Brain Tissue Mechanical Properties," in *Biomechanics of the Brain*, K. Miller, Ed., in Biological and Medical Physics, Biomedical Engineering. , New York, NY: Springer, 2011, pp. 69–89. doi: 10.1007/978-1-4419-9997-9_4.

[34] S. A. Bentil and R. B. Dupaix, "Simulations of hydrogel-coated neural microelectrodes to assess biocompatibility improvement using strain as a metric for micromotion," *Biomed. Phys. Eng. Express*, vol. 4, no. 3, p. 035036, Apr. 2018, doi: 10.1088/2057-1976/aab990.

[35] M. Mariello, K. Kim, K. Wu, S. P. Lacour, and Y. Leterrier, "Recent Advances in Encapsulation of Flexible Bioelectronic Implants: Materials, Technologies, and Characterization Methods," *Adv. Mater.*, vol. 34, no. 34, p. 2201129, 2022, doi: 10.1002/adma.202201129.

[36] T. Araki *et al.*, "Flexible neural interfaces for brain implants—the pursuit of thinness and high density," *Flex. Print. Electron.*, vol. 5, no. 4, p. 043002, Nov. 2020, doi: 10.1088/2058-8585/abc3ca.

[37] E. Musk and Neuralink, "An integrated brain-machine interface platform with thousands of channels," *bioRxiv*, p. 703801, Aug. 2019, doi: 10.1101/703801.

[38] L. Luan *et al.*, "Ultraflexible nanoelectronic probes form reliable, glial scar–free neural integration," *Sci. Adv.*, vol. 3, no. 2, p. e1601966, Feb. 2017, doi: 10.1126/sciadv.1601966.

[39] "Mechanically Matched Silicone Brain Implants Reduce Brain Foreign Body Response - Zhang - 2021 - Advanced Materials Technologies - Wiley Online Library." Accessed: May 12, 2023. [Online]. Available: https://onlinelibrary-wiley-com.erl.lib.byu.edu/doi/full/10.1002/admt.202000909?casa_token=OeEy33sLN3oAAAAA%3ADXSly d0ualD3yPX9wGtdT-1hukrcxnUobsJ1ZW8WBkBnZJ-9gKCNeHYZG7oSqrt6dxIeHXEFM2t8HgU

[40] W. C. Fazio, J. M. Lund, T. S. Wood, B. D. Jensen, R. C. Davis, and R. R. Vanfleet, "Material Properties of Carbon-Infiltrated Carbon Nanotube-Templated Structures for Microfabrication of Compliant Mechanisms," presented at the ASME 2011 International Mechanical Engineering Congress and Exposition, American Society of Mechanical Engineers Digital Collection, Aug. 2012, pp. 481–490. doi: 10.1115/IMECE2011-64168.

[41] D. N. Hutchison *et al.*, "Carbon Nanotubes as a Framework for High-Aspect-Ratio MEMS Fabrication," *J. Microelectromechanical Syst.*, vol. 19, no. 1, pp. 75–82, Feb. 2010, doi: 10.1109/JMEMS.2009.2035639.

[42] G. Chen *et al.*, "Fabrication of High Aspect Ratio Millimeter-Tall Free-Standing Carbon Nanotube-Based Microelectrode Arrays," *ACS Biomater. Sci. Eng.*, vol. 4, no. 5, pp. 1900–1907, May 2018, doi: 10.1021/acsbiomaterials.8b00038.

[43] B. R. C. de Menezes, K. F. Rodrigues, B. C. da S. Fonseca, R. G. Ribas, T. L. do A. Montanheiro, and G. P. Thim, "Recent advances in the use of carbon nanotubes as smart biomaterials," *J. Mater. Chem. B*, vol. 7, no. 9, pp. 1343–1360, Feb. 2019, doi: 10.1039/C8TB02419G.

[44] K. Foremny *et al.*, "Carbon-Nanotube-Coated Surface Electrodes for Cortical Recordings In Vivo," *Nanomaterials*, vol. 11, no. 4, Art. no. 4, Apr. 2021, doi: 10.3390/nano11041029.

[45] G. H. Kim *et al.*, "CNT-Au nanocomposite deposition on gold microelectrodes for improved neural recordings," *Sens. Actuators B Chem.*, vol. 252, pp. 152–158, Nov. 2017, doi: 10.1016/j.snb.2017.04.142.

[46] T. Palomäki *et al.*, "Unmodified and multi-walled carbon nanotube modified tetrahedral amorphous carbon (ta-C) films as in vivo sensor materials for sensitive and selective detection of dopamine," *Biosens. Bioelectron.*, vol. 118, pp. 23–30, Oct. 2018, doi: 10.1016/j.bios.2018.07.018.

[47] W. Harreither, R. Trouillon, P. Poulin, W. Neri, A. G. Ewing, and G. Safina, "Carbon Nanotube Fiber Microelectrodes Show a Higher Resistance to Dopamine Fouling," *Anal. Chem.*, vol. 85, no. 15, pp. 7447–7453, Aug. 2013, doi: 10.1021/ac401399s.

[48] H. J. Johnston *et al.*, "A critical review of the biological mechanisms underlying the in vivo and in vitro toxicity of carbon nanotubes: The contribution of physico-chemical characteristics," *Nanotoxicology*, vol. 4, no. 2, pp. 207–246, 2010, doi: 10.3109/17435390903569639.

[49] B. M. Popescu, N. Ali, G. Basturea, G. I. Comsa, L. A. Materon, and M. Chipara, "1-Dimensional nanoparticles – A brief critical review on biological, medical, and toxicological aspects," *Appl. Surf. Sci.*, vol. 275, pp. 2–6, Jun. 2013, doi: 10.1016/j.apsusc.2013.01.122.

[50] M. Razavi and A. Khandan, "14 - Safety, regulatory issues, long-term biotoxicity, and the processing environment," in *Nanobiomaterials Science, Development and Evaluation*, M. Razavi and A. Thakor, Eds., Woodhead Publishing, 2017, pp. 261–279. doi: 10.1016/B978-0-08-100963-5.00014-8.

[51] Y. Li and J. Cao, "The impact of multi-walled carbon nanotubes (MWCNTs) on macrophages: contribution of MWCNT characteristics," *Sci. China Life Sci.*, vol. 61, no. 11, pp. 1333–1351, Nov. 2018, doi: 10.1007/s11427-017-9242-3.

[52] D. A. Heller *et al.*, "Banning carbon nanotubes would be scientifically unjustified and damaging to innovation," *Nat. Nanotechnol.*, vol. 15, no. 3, Art. no. 3, Mar. 2020, doi: 10.1038/s41565-020-0656-y.

[53] K. Kostarelos, "The long and short of carbon nanotube toxicity," *Nat. Biotechnol.*, vol. 26, no. 7, Art. no. 7, Jul. 2008, doi: 10.1038/nbt0708-774.

[54] C. Redondo-Gómez, R. Leandro-Mora, D. Blanch-Bermúdez, C. Espinoza-Araya, D. Hidalgo-Barrantes, and J. Vega-Baudrit, "Recent Advances in Carbon Nanotubes for Nervous Tissue Regeneration," Jul. 2019, doi: 10.20944/preprints201907.0245.v1.

[55] S. Sharma and M. J. Madou, "Micro and nano patterning of carbon electrodes for bioMEMS," 2012. doi: 10.1680/bbn.12.00010.

[56] D. A. X. Nayagam *et al.*, "Biocompatibility of Immobilized Aligned Carbon Nanotubes," *Small*, vol. 7, no. 8, pp. 981–981, 2011, doi: 10.1002/smll.201190025.

[57] R. A. Dubin, G. C. Callegari, J. Kohn, and A. V. Neimark, "Carbon Nanotube Fibers Are Compatible With Mammalian Cells and Neurons," *IEEE Trans. NanoBioscience*, vol. 7, no. 1, pp. 11–14, Mar. 2008, doi: 10.1109/TNB.2008.2000144.

[58] A. Vega-Estrada *et al.*, "Biocompatibility and Biomechanical Effect of Single Wall Carbon Nanotubes Implanted in the Corneal Stroma: A Proof of Concept Investigation," *J. Ophthalmol.*, vol. 2016, 2016, doi: 10.1155/2016/4041767.

[59] A. S. Kishore, P. Surekha, and P. B. Murthy, "Assessment of the dermal and ocular irritation potential of multi-walled carbon nanotubes by using in vitro and in vivo methods," *Toxicol. Lett.*, vol. 191, no. 2–3, pp. 268–274, 2009, doi: 10.1016/j.toxlet.2009.09.007.

[60] A. Huczko and H. Lange, "Carbon nanotubes: Experimental evidence for a null risk of skin irritation and allergy," *Fuller. Sci. Technol.*, vol. 9, no. 2, pp. 247–250, 2001, doi: 10.1081/FST-100102972.

[61] Y. Hanein and L. Bareket-Keren, "Carbon nanotube-based multi electrode arrays for neuronal interfacing: progress and prospects," *Front. Neural Circuits*, vol. 6, 2013, Accessed: Sep. 06, 2022. [Online]. Available: https://www.frontiersin.org/articles/10.3389/fncir.2012.00122

[62] C. by M. Ströck, *English: This illustration depicts eight of the allotropes (different molecular configurations) that pure carbon can take:* 2006. Accessed: Apr. 13, 2020. [Online]. Available: https://commons.wikimedia.org/wiki/File:Eight_Allotropes_of_Carbon.png

[63] "Carbon nanotube," *Wikipedia*. Mar. 25, 2020. Accessed: Mar. 25, 2020. [Online]. Available: https://en.wikipedia.org/w/index.php?title=Carbon_nanotube&oldid=947343415

[64] J. Song *et al.*, "Carbon-Nanotube-Templated Microfabrication of Porous Silicon-Carbon Materials with Application to Chemical Separations," *Adv. Funct. Mater.*, vol. 21, no. 6, pp. 1132–1139, 2011, doi: https://doi.org/10.1002/adfm.201001851.

[65] Y. Y. Wei, G. Eres, V. I. Merkulov, and D. H. Lowndes, "Effect of catalyst film thickness on carbon nanotube growth by selective area chemical vapor deposition," *Appl. Phys. Lett.*, vol. 78, no. 10, pp. 1394–1396, Feb. 2001, doi: 10.1063/1.1354658.

[66] "Ostwald ripening," *Wikipedia*. Mar. 25, 2020. Accessed: Mar. 25, 2020. [Online]. Available: https://en.wikipedia.org/w/index.php?title=Ostwald_ripening&oldid=947295528

[67] R. Brukh and S. Mitra, "Mechanism of carbon nanotube growth by CVD," *Chem. Phys. Lett.*, vol. 424, no. 1, pp. 126–132, Jun. 2006, doi: 10.1016/j.cplett.2006.04.028.

[68] J.-P. Tessonnier and D. S. Su, "Recent Progress on the Growth Mechanism of Carbon Nanotubes: A Review," *ChemSusChem*, vol. 4, no. 7, pp. 824–847, Jul. 2011, doi: 10.1002/cssc.201100175.

[69] B. H. Hanna *et al.*, "Mechanical Property Measurement of Carbon Infiltrated Carbon Nanotube Structures for Compliant Micromechanisms," *J. Microelectromechanical Syst.*, vol. 23, no. 6, pp. 1330–1339, Dec. 2014, doi: 10.1109/JMEMS.2014.2312847.

[70] K. Laughlin, R. R. Vanfleet, and R. C. Davis, "Mechanically Robust Vertically Aligned Carbon Nanotube Composites for Applications in Ultralow Reflectance Optical Elements," *ACS Appl. Nano Mater.*, vol. 5, no. 5, pp. 6989–6994, May 2022, doi: 10.1021/acsanm.2c00947.

[71] "Euler–Bernoulli beam theory," *Wikipedia*. Mar. 04, 2020. Accessed: Apr. 16, 2020. [Online]. Available: https://en.wikipedia.org/w/index.php?title=Euler%E2%80%93Bernoulli_beam_theory&oldid=94388 3619

[72] M. Polanco, S. Bawab, and H. Yoon, "Computational Assessment of Neural Probe and Brain Tissue Interface under Transient Motion," *Biosensors*, vol. 6, no. 2, p. 27, Jun. 2016, doi: 10.3390/bios6020027.

[73] M. Polanco, H. Yoon, and S. Bawab, "Micromotion-induced dynamic effects from a neural probe and brain tissue interface," *J. MicroNanolithography MEMS MOEMS*, vol. 13, no. 2, p. 023009, Jun. 2014, doi: 10.1117/1.JMM.13.2.023009.

[74] S. Budday, T. C. Ovaert, G. A. Holzapfel, P. Steinmann, and E. Kuhl, "Fifty Shades of Brain: A Review on the Mechanical Testing and Modeling of Brain Tissue," *Arch. Comput. Methods Eng.*, vol. 27, no. 4, pp. 1187–1230, Sep. 2020, doi: 10.1007/s11831-019-09352-w.

[75] J. Subbaroyan, D. C. Martin, and D. R. Kipke, "A finite-element model of the mechanical effects of implantable microelectrodes in the cerebral cortex," *J. Neural Eng.*, vol. 2, no. 4, pp. 103–113, Dec. 2005, doi: 10.1088/1741-2560/2/4/006.

[76] Z. Wang, A. A. Volinsky, and N. D. Gallant, "Crosslinking effect on polydimethylsiloxane elastic modulus measured by custom-built compression instrument," *J. Appl. Polym. Sci.*, vol. 131, no. 22, 2014, doi: 10.1002/app.41050.

[77] P. P. S. S. Abadi, M. R. Maschmann, J. W. Baur, S. Graham, and B. A. Cola, "Deformation response of conformally coated carbon nanotube forests," *Nanotechnology*, vol. 24, no. 47, p. 475707, Nov. 2013, doi: 10.1088/0957-4484/24/47/475707.

[78] A. Mariet, A. T. Perez Fontenla, X. Gabrion, C. Salomon, R. Veness, and M. Devel, "Mechanical characterization of yarns made from carbon nanotubes for the instrumentation of particle beams at CERN," *Nucl. Instrum. Methods Phys. Res. Sect. Accel. Spectrometers Detect. Assoc. Equip.*, vol. 1036, p. 166867, Aug. 2022, doi: 10.1016/j.nima.2022.166867.

[79] P. P. A, V. Rajamohan, and A. T. Mathew, "Material and Mechanical Characterization of Multi-Functional Carbon Nanotube Reinforced Hybrid Composite Materials," *Exp. Tech.*, vol. 43, no. 3, pp. 301–314, Jun. 2019, doi: 10.1007/s40799-019-00316-0.

[80] L. Lattanzi, L. De Nardo, J. R. Raney, and C. Daraio, "Geometry-Induced Mechanical Properties of Carbon Nanotube Foams," *Adv. Eng. Mater.*, vol. 16, no. 8, pp. 1026–1031, 2014, doi: 10.1002/adem.201300524.

[81] X. Liang *et al.*, "Compression and recovery of carbon nanotube forests described as a phase transition," *Int. J. Solids Struct.*, vol. 122–123, pp. 196–209, Sep. 2017, doi: 10.1016/j.ijsolstr.2017.06.025.

[82] N. J. Ginga and S. K. Sitaraman, "The experimental measurement of effective compressive modulus of carbon nanotube forests and the nature of deformation," *Carbon*, vol. 53, pp. 237–244, Mar. 2013, doi: 10.1016/j.carbon.2012.10.054.